의학박사 학위논문

Ultrasound-guided photoacoustic imaging for diagnosis and near infrared photothermal therapy of triple negative breast cancer using EGFR antibody-conjugated gold nanorods

EGFR항체접합 골드나노입자를 이용한 삼중음성유방암 표적지향 광초음파 영상진단과 근적외선치료에 관한 연구

2017년 8월

서울대학교 대학원

의과학과

MEIHUA ZHANG

A thesis of the Degree of Doctor of Philosophy

EGFR항체접합 골드나노입자를 이용한 삼중음성유방암 표적지향 광초음파 영상진단과 근적외선치료에 관한 연구

Ultrasound-guided photoacoustic imaging for diagnosis and near infrared photothermal therapy of triple negative breast cancer using EGFR antibody-conjugated gold nanorods

August 2017

The Department of Biomedical Sciences,

Seoul National University

College of Medicine

MEIHUA ZHANG

ABSTRACT

Introduction: Triple negative breast cancer (TNBC), lacking human epidermal growth factor receptor 2 (HER2), and estrogen receptor (ER) and progesterone receptor (PR) expression, are associated with an aggressive natural history compared with other disease subtypes. Approximately 70 to 80% of TNBCs more frequently overexpress the epidermal growth factor receptor (EGFR), which is emerging as a therapeutic target. Photoacoustic imaging (PAI), which can create multi-contrast images of living biological structures ranging from organelles to organs, has shown great translational potential from bench to bedside due to it being relatively inexpensive and convenient for combination with clinical ultrasound (US). Gold nanorods (GNs) are extensively used for PAI and NIR-PTT. The first aim of this study is to assess the use of US-guided PAI and anti-EGFR antibody-conjugated GNs (anti-EGFR-GNs) to detect the EGFR-expressing primary tumor mass and regional LN metastases in a mouse model of human TNBC. Secondary aim of this study is to prove that anti-EGFR-GNs combined with NIR-PTT is an encouraging therapeutic strategy for highly selective cancer cell targeting and synergistic anti-cancer activity in aggressive TNBCs.

Methods: The human breast cancer cell lines (ER+) subtype;MCF-7, HER2+ subtype; BT-474, and TN subtype; HCC-578T, HCC-38, HCC-1937, MDA-MB-453 and MDA-MB-231) were used. The intracellular signaling events were evaluated by Western blot. Cell proliferation activity was evaluated by MTT assay.

For analysis of apoptotic cell damage, fluorescence of annexin V and propidium iodide was measured using flow cytometry. MDA-MB-231 and MCF-7 cells were fat pad injected into the back right flank of female BALB/c nude mice (4-5 week old) for xenograft tumor model. GNs and anti-EGFR-GNs, 10 nm in diameter and 41 nm in length used as PAI contrast agents. *In vivo* real-time US-guided PAI and bioluminescence imaging of primary tumor and LN were performed using a preclinical Vevo 2100 LAZR Imaging system and IVIS Lumina II Imaging system, respectively. For the study of anti-EGFR-GNs-combined NIR-PTT heat (up to 43°C) of the culture medium and tumor skin was produced by irradiation of a water-filtered infrared A lamp (at 1.5 W/cm2) for 3 min at 48 h post-treatment with anti-EGFR-GNs. Hematoxylin and eosin staining, silver enhancement staining, and immunostaining were performed on tissue sections.

Results: Representative western blots showed that TNBC cell lines (Hs578T, HCC-38, HCC-1937, MDA-MB-468 and MDA-MB-231) highly expressed EGFR whereas the other ER+ (MCF-7) and HER2+ cell lines (BT474) did not. A large amount of nanoparticles in the intracellular region was apparent in MDA-MB-231 cells treated with anti-EGFR-GNs for 24 h, whereas very few nanoparticles in the cytoplasm were observed in the MDA-MB-231 cells treated with GNs. In the EGFR-targeting study in cultured MCF-7 and MDA-MB-231 cells, selective binding of anti-EGFR-GNs on MDA-MB-231 cells which highly expressed EGFR was evident, but no binding observed in MCF-7 cells. Intratumor injection of anti-EGFR-GNs provided a significant enhancement in PA signal in axillary LN of mice

after 24h, which correlated histologically with LN metastases with small number of cancer cells and anti-EGFR-GNs accumulation. The treatment of anti-EGFR-GNs combined with NIR-PTT augmented the induction of HSP70 and cleaved caspase-3 and decreased Ki-67 and EGFR and EGFR accompanying the strong inhibition of intracellular signaling molecules (mTOR, AKT, ERK1/2, and FAK), eventually exerting synergic anti-proliferative and apoptotic effects on the MDA-MB-231 cells. With the help of longitudinal real-time US-guided PAI and bioluminescence imaging, the combination of NIR-PTT, after three intravenous injections of anti-EGFR-GNs in tumor models, resulted in the greatest therapeutic effectiveness of almost complete tumor regression without virtually normal tissue damage compared with the treatment responses with free anti-EGFR antibodies or anti-EGFR-GNs alone.

Conclusions: In conclusion, US-guided PAI technology using anti-EGFR-GNs is feasible and highly sensitive for the selective visualization of EGFR-targeted primary tumors as well as LN micrometastases in a murine model of human TNBC. Anti-EGFR-GNs combined with NIR-PTT is an effective therapeutic strategy for TNBC, which enables selective tumor cell targeting through the synergistic mechanism of anti-proliferation and apoptosis without side effects and complications compared with previous conventional therapy strategy for EGFR-overexpressing TNBCs.

Keywords: Photoacoustic imaging: Gold nanorod； Epidermal growth factor receptor； Indocyanine green； Ultrasound imaging；Lymph node metastases；Triple negative breast cancer； Near Infrared； Photothermal Therapy.

Student number: 2014-30871

CONTENTS

LIST OF TABLES AND FIGURES

LIST OF ABBREVIATIONS

anti-EGFR-GNs: antibody-conjugated gold nanorods

NIR-PTT: near infrared photothermal therapy

TNBC: triple negative breast cancer

US: ultrasound

PAI: photoacoustic imaging

LN: lymph node

ER+: estrogen receptor positive

HER2+: human epidermal growth factor receptor 2

BLI: bioluminescence imaging

TEM: transmission electron microscopy

INTRODUCTION

Breast cancer is a heterogeneous disease comprising several biologically distinct subtypes, and the majority of breast cancer-related deaths are mainly due to incurable metastatic diseases [1]. Triple negative breast cancer (TNBC), lacking human epidermal growth factor receptor 2 (HER2), and estrogen receptor (ER) and progesterone receptor (PR) expression, are associated with an aggressive natural history compared with other disease subtypes. Although triple negative breast cancer (TNBC) is a small percentage of all breast cancers, to date, TNBC is one of the most challenging types of breast cancer for basic and clinic research because TNBC patients display a high risk of relapse, shorter overall survival and limited therapeutic options after completion of conventional chemotherapy compared with patients with other breast cancer subtypes [2, 3]. Because of the lack of a well-defined clinical strategy, chemotherapy is currently the standard-of-care therapy for TNBC patients. Advances in the design of strategies for the treatment of TNBC require further elucidation, by combined targeted therapy, of the molecular mechanisms underlying TNBC genotypic and phenotypic heterogeneity. Approximately 70 to 80% of TNBCs more frequently overexpress the epidermal growth factor receptor (EGFR), which correlated with a more aggressive phenotype and poor clinical outcomes [4, 5]. Targeting the epidermal growth factor receptor (EGFR) has been proposed as a promising imaging biomarker for selective detection and treatment of EGFR-positive TNBC including metastases, but it is still in the early stages [6-8]. Many clinical studies on TNBC patients using an EGFR antibody (cetuximab) and EGFR pathway inhibitors (lapatinib and gefitinib) combined with chemotherapy have been evaluated to date, yet EGFR-targeted therapy has produced a response in only a minority of TNBC patients [6, 9]. A rational

therapeutic strategy to overcome the limitations and complications of current treatments of TNBC patients is absolutely required for future clinical trials.

Non-invasive monitoring of tumors *in vivo* with biocompatible contrast agents including specific targeting molecules after multiple rounds of intravenous administration may be capable of being optimized and an efficacious treatment of cancer. Photoacoustic imaging (PAI), which can create multicontrast images of living biological structures ranging from organelles to organs, has shown great translational potential from bench to bedside due to it being relatively inexpensive and convenient for combination with clinical ultrasound (US) [10]. Photoacoustic imaging (PAI), which uses the phenomena of optical absorption, rapid thermoelastic expansion, and acoustic pressure wave generation, has been introduced as a modality that can break through the fundamental limitation of the existing pure optical imaging techniques and can be performed using various endogenous and exogenous contrast agents [10]. PAI systems have been commercialized to meet the growing demand for studying models of human disease in small animals due to the availability of relatively inexpensive and convenient tools for clinical application. Recently, ultrasound (US)-guided functional PAI using exogenous contrast agents was introduced as a promising approach for the more sensitive and accurate detection of tumor and lymph node (LN) metastases *in vivo* [11-13]. Gold nanoparticles with strong optical absorption in the near-infrared spectral range are developed as PA contrast agents to obtain target-specific information on molecular or cellular processes with high sensitivity and specificity, offering considerable advances in preclinical research and clinical applications, especially in oncology [10, 12]. Gold nanoparticles have been shown to be non-toxic to human cells, but are still undergoing initial investigation in clinical cancer trials [14-16]. In recent years, gold nanorods (GNs) with distinctive rod shape-dependent optical properties

have been proposed as attractive antibody conjugated PA contrast agents to enable the selective detection of primary tumor and metastases *in vivo* [16-18]. GNs with particularly near-infrared (NIR) optical properties at wavelengths from 700 to 1000 nm, where NIR radiation is able to penetrate the skin without damaging normal tissues, have revealed great potential for simultaneously combining selective targeted imaging and NIR-mediated photothermal therapy (NIR-PTT) in diverse types of cancer [19-22]. In recent years, NIR-PTT using GNs embedded within tumors can cause apoptotic or necrotic damage to tumor cells by inducing a localized hyperthermia effect, suggesting a promising therapeutic technique with great potential for cancer treatment due to its minimal invasiveness and high spatial selectivity [23-29]. To date, GNs heated with an NIR light have improved the efficiency and safety of therapy against various solid tumors, yet few studies have demonstrated the successful treatment of TNBC.

Anti-EGFR-GNs with a desired NIR wavelength (approximately 808 nm) are ideal for both cancer cell imaging and NIR-PTT. Taken together, US-guided PA imaging technology using anti-EGFR-GNs is feasible and highly sensitive to allow selective visualization of EGFR-targeted primary tumor as well as LN micrometastases in a murine model of human TNBC. We evaluated the feasibility of using anti-EGFR-GNs combined with NIR-PTT for most effective EGFR-targeted therapy of TNBCs with the help of non-invasive and real-time monitoring of selective targeting as well as therapeutic response using US-guided PAI.

MATERIALS AND METHODS

1. GNs and anti-EGFR-GNs

GNs and anti-EGFR-GNs (10 nm×40 nm) were purchased from Nanopartz, Inc. (Loveland, CO, USA). In brief, highly stable cetyltrimethylammonium bromide (CTAB)-coated GNs with longitudinal plasmon resonance at 808 nm were synthesized using a proprietary seed growth method. An SH-terminated branched amine polymer manufactured by Nanopartz was used to replace the CTAB. BS3 chemistry was used to attach the amine polymer to the primary amine of the anti-EGFR antibodies. It was calculated that there are over 100 amines/nm^2, which results in loading of 16 antibodies per GN. Centrifugation and dialysis against sterile phosphate buffered saline were used in all steps of binding and purification. Loading of antibodies was determined using a proprietary method incorporating HPLC and UVVIS. Further sterilization and endotoxin testing was performed.

2. Cell culture and reagents

The following human breast cancer cell lines were obtained from the Korean Cell Line Bank (Seoul, Korea): estrogen receptor positive (ER+) cell line (MCF-7), human epidermal growth factor receptor 2 amplified (HER2+) cell line (BT-474) and TNBC cell lines (Hs578T, HCC-38, HCC-1937, MDA-MB-453 and MDA-MB-231). The Hs578T, HCC-38, HCC-1937, MDA-MB-453 and MDA-MB-231 cell lines were grown in RPMI1640 medium (WelGENE, Daegu, Korea) containing 10% FBS and supplemented with a 1% antibiotic solution containing penicillin and streptomycin. The BT-474 and MCF-7 cells were grown in DMEM (WelGENE, Daegu, Korea) containing 10% FBS and supplemented with a 1% antibiotic solution containing

penicillin and streptomycin. MDA-MB-231-Luc cells stably expressing firefly luciferase were established using lentivirus.

3. 3-(4,5-Dimethylthiazol-2-yl)-2,5-diphenyl tetrazolium bromide (MTT) assay

In vitro cell viability and proliferation were assessed using the MTT assay. Briefly, 5×10^3 cells were allowed to adhere in a high humidity environment in 5% CO_2 at 37 °C in 96-well culture plates. Following a 24 h incubation period, cells were treated with GNs, anti-EGFR-GNs, anti-EGFR and EGF for an additional 24 h, 48 h, and 72 h. After washing cells with PBS, the medium was replaced with fresh culture medium; the MTT solution (final concentration of 1 mg/ml) was added, and the cells were incubated for 1 h. At the end of the incubation period, the MTT solution was carefully removed, and 150 µl of dimethyl sulfoxide was added to each well. The plates were maintained on a rocker shaker for 10 min at 25 ℃, and then the amount of MTT formazan crystals formed by the viable cells was determined using a spectrophotometer based on the absorbance at 540 nm (GE Healthcare, Piscataway, NJ, USA).

4. Flow cytometry

For investigating cell damage by anti-EGFR-GN treatment alone or the combination anti-EGFR-GNs and NIR-PTT, flow cytometry was performed using a FACS Calibur flow cytometer (BD Biosciences, San Jose, CA, USA). The cells were cultured in 6-well plates and subsequently treated with anti-EGFR-GNs, anti-EGFR alone or in combination with NIR. The cells were collected and washed twice with ice-cold PBS containing 1% BSA and 1 mM EDTA and incubated with annexin V and propidium iodide (BD Biosciences, San Jose, CA, USA) for 10 min at room temperature. Cell damage was assessed concomitantly with flow cytometric evaluation of cells stained by annexin V, and propidium iodide-associated fluorescence was

measured. The data were analyzed using Cell Quest v3.3 software (BD Biosciences, San Jose, CA, USA).

5. Western blotting analysis

The cells were lysed in RIPA buffer (Sigma, St. Louis, MO, USA). Proteins were separated using SDS-polyacrylamide gel electrophoresis (SDS-PAGE) and transferred to nitrocellulose membranes. The membranes were blocked using 5% skim milk in Tris-buffered saline containing 0.05% Tween-20 and were incubated with primary antibodies overnight at 4°C, followed by incubation with a horseradish peroxidase-conjugated secondary antibody (Santa Cruz Biotechnology, Santa Cruz, CA, USA) at room temperature for 30 min. The following primary antibodies were used in this study: anti-EGFR, anti-phospho-AKT, anti-AKT, anti-phospho-ERK1/2, anti-ERK1/2, anti-phospho-mTOR, anti-mTOR, anti-cleaved caspase-3 and anti-FAK antibodies purchased from Cell Signaling Technology (Danvers, MA, USA), anti-phospho-FAK and anti-β-actin antibodies purchased from Sigma (St. Louis, MO, US), anti-HSP70 and anti-HSP90 antibodies purchased from Abcam (Cambridge, MA, USA), and Ki-67 antibody purchased from Santa Cruz Biotechnology (Santa Cruz, CA, USA). The blots were developed using Enhanced Chemiluminescence Reagents (Amersham Biosciences, Piscataway, NJ, USA). The relative intensity of the bands observed by Western blotting was analyzed using the Image J program.

6. Immunocytochemistry

Cells were directly cultured on 8-well chamber slides (Lab-Tek chamber slide), fixed in 4% paraformaldehyde, and blocked with 2% bovine serum albumin. After washing, the cells were incubated with the anti-EGFR antibody (Cell Signaling Technology, Danvers, MA, USA) at 4°C overnight, followed by incubation with an

appropriate secondary antibody for 1 h at room temperature. The proteins were visualized with 3,3-diaminobenzidine (DAB), and hematoxylin was used as counterstain. The images were acquired using a microscope equipped with a CCD camera (Leica, Wetzlar, Germany).

7. Transmission electron microscopy (TEM)

For the TEM observation of the intracellular distribution of anti-EGFR-GNs, cells were incubated with 10 ml of medium containing 120 pmol/L of anti-EGFR-GNs for 24 h. Collected cells were fixed with 2.5% glutaraldehyde, treated with 2% osmium tetroxide in 0.1 mM cacodylate buffer for 2 h, dehydrated with graded ethanol from 50 to 100% and propylene oxide and embedded in pure Epon resin at 60 ºC for 3 days. Ultrathin sections were cut with glass knives and a Diatome diamond knife (Reichert-Jung, Vienna, Austria) using an ultramicrotome (RMC MTXL; Tucson, AZ, USA), stained with lead citrate and uranyl acetate and observed with a JEM-100 CX transmission electron microscope (JEOL, Tokyo, Japan).

8. Xenograft tumor model

All animal experiments were approved by the Seoul National University Hospital Biomedical Research Institute Animal Care and Use Committee (IACUC). A total of 46 female Balb/c nude mice (5-6 weeks old) were used for PA and US imaging and histological studies. For developing the tumor model, 1×10^6 viable MDA-MB-231-Luc cells were suspended in 0.1 ml of Matrigel (BD Biosciences, Franklin Lakes, NJ, USA) and injected into the right fat pad and were injected into the 4th mammary gland of mice. Tumor formation was monitored for 4-6 weeks after implantation. To monitor primary tumor growth and metastases non-invasively, the luciferase bioluminescence images were obtained and quantified using an *in vivo* bioluminescence imaging system.

Tumor volume was measured with calipers and by US imaging using a modified ellipsoidal formula for volume (volume = 1/2[length×width^2]) [30]. Indocyanine green (ICG) (Sigma-Aldrich, St Louis, MI, USA), non-targeted GN, and anti-EGFR-GNs (10 nm×40 nm, Nanopartz Inc., Lovel, CO, USA) were dissolved in physiological buffered solution. Six healthy mice were randomly assigned to one of 2 experimental groups, those that received an ICG injection (n=3) and those that received a GN injection (n=3). To identify and image the axillary LN of mice, 30μl of ICG (1 mM, final 5pmol/g mouse) or GN (1 nM, final 0.005 pmol/g mouse) was injected into the right forepaw pad of each mouse, a 3-4 mm thick section of chicken breast tissue was overlaid on the axillary LN, and the mouse was imaged using PA and US imaging.

When the average tumor volume of 20 tumor-bearing mice injected with either MDA-MB-231 cells (MDA-MB-231 tumor) or MCF-7 cells (MCF-7 tumor) reached 150-200 mm^3, the mice were randomly assigned to one of 4 experimental groups and were injected intravenously via a tail vein with either 100μl of GN (100 nM, final 0.5 pmol/g mouse) or anti-EGFR-GNs (100 nM, final 0.5 pmol/g mouse): group 1, MDA-MB-231 tumor-GN(n=5); group 2, MCF-7 tumor-GN(n=5); group 3, MDA-MB-231 tumor-anti-EGFR-GN(n=5); and group 4, MCF-7 tumor-anti-EGFR-GN(n=5). The mice were then imaged using non-invasive PA and US imaging.

To identify and image the axillary LN metastases from MDA-MB-231/Luc-tumor-bearing mice (n=6) at 8 weeks, 100μl of anti-EGFR-GNs (100 nM, final 0.5 pmol/g mouse) was injected in to the primary tumor, and 150ug/g of D-luciferin (Promega, San Luis Obispo, CA, USA) was injected into the peritoneum, followed by bioluminescence, PA and US imaging.

To identify and image the Tumor treatment effect, the mice were randomly assigned to one of 4 experimental groups: group 1, saline (control) (n=5); group 2, anti-EGFR-GNs only (n=5); group 3, anti-EGFR-GNs + NIR-PTT (n=5); and group 4, anti-EGFR only (n=5). The tumor volumes of each group were non-invasively monitored after three intravenous injections with either 100 μl of anti-EGFR-GNs (100 nM, final of 0.5 pmol/g mouse) or anti-EGFR (100 nM, final of 0.5 pmol/g mouse) and the combination with NRI-PTT.

9. Bioluminescent imaging

In vivo bioluminescent imaging (BLI) was conducted on the IVIS luminal II system (Caliper, Hopkinton, MA, USA) with the use of Living Image acquisition and analysis software. The mice were anesthetized with isoflurane after which they were intraperitoneally injected with 150 μg/g of the firefly luciferase substrate, D-luciferin (Promega, San Luis Obispo, CA, USA). To capture peak intensity, imaging of the tumor and LN area was conducted 10 min after the injection of D-luciferin to capture the peak intensity, which could well represent the primary tumor volume and the metastatic nodule area in the LN. Bioluminescence imaging was performed 4, 5, 6, 7 and 8 weeks after injection with 1×10^6 MDA-MB-231/Luc cells stably expressing firefly luciferase. 1^{st}, 2^{nd} and 3^{rd} treatment after, bioluminescence imaging was performed. The sum of all detected photon counts within tumor was quantified in units of mean photons per second per centimeter squared per steradian ($p/s/cm^2/sr$).

10. PA and US imaging

All *in vivo* imaging studies were performed in PA mode using a small-animal high resolution Vevo2100 LAZR high frequency US and PA imaging system (FUJIFILM VisualSonics Inc., Toronto, Ontario, Canada). A linear array transducer (LZ-550, 32-

55 MHz center frequency linear array with integrated light source) was used to acquire all PA and US images. In this system, integrated fiber optic transducers are employed to deliver nanosecond laser pulses into deep anatomical targets. Tissues differentially and specifically absorb the light causing transient thermoelastic expansions, generating acoustic pressure waves, which are detected by 256 sensitive piezoelectric elements. Transmitted US pulses are similarly received, generating high-resolution images of microscopic anatomical structures. The photoacoustic and spatial dimensions of the collected US images were <14 mm (width) by <15 mm (depth). Clear gel was centrifuged (to remove air bubbles) and used to provide PA coupling between the probe and tumor. The laser was tuned to optical wavelengths from 750 to 850 nm with a PA signal gain of 40 dB. Data were collected in triplicate at a frame rate of 5 Hz for 20 s. Laser fluence, measured by a Nova II power meter with a PE50BB sensor (Ophir-Spiricon, LLC, North Logan, UT, USA), was between 10 and 20 mJ/cm^2; all laser energies were below the American National Standards Institute (ANSI) safe exposure level for human skin. PA images were averaged eight times, thus suppressing uncorrelated noise. Images were analyzed using post-processing software tools (FUJIFILM VisualSonics Inc., Toronto, Ontario, Canada). Tumor boundaries, as identified on the digitally stored US images, were outlined manually for quantification of the PA signal over the area. Each PA image was normalized by the measured fluence to correct for the pulse-to-pulse laser energy variations.

11. NIR-PTT using anti-EGFR-GNs

Heat was applied using a wIRA (Hydrosun model 750, Hydrosun Medizintechnik GmbH, Müllheim, Germany) with a 750 watt halogen lamp and a 780 nm high pass filter, yielding a peak output at 820 nm. *In vitro* NIR-PTT (at 1.5 W/cm^2 for 3 min) was performed in cultured cells at 24 h after treatment with anti-EGFR, GN, or anti-

EGFR-GN. Based on our previous study [31], we decided NIR-PTT time point at which anti-EGFR-GNs were maximally accumulated into the tumors of mice after intravenous injection of anti-EGFR-GNs using serial follow-up PAI. When the average tumor volume was 150-200 mm^3, a circular mask 1.5 cm in diameter was placed over the abdomen to confine the radiation to the tumor region and *in vivo* NIR-PTT (at 1.5 W/cm2 for 3 min) at 48 h after intravenous injection of anti-EGFR-GNs (100 nM, final 0.5 pmol/g mouse) at 3 d-intervals was performed three times. The temperature of culture medium and tumor skin was measured using the non-contact infrared thermometer gun (BENETECH, Shenzhen, China)

12. Histological analysis

Histological analyses of axillary LN and primary tumors were performed. The axillary LN was removed after injection of ICG or non-targeted GN. The tumors and organs were removed 48 h after the injection of non-targeted GN or anti-EGFR-GNs. The metastases detection of axillary LN was removed 48 h after the injection of anti-EGFR-GNs. The tumors and organs (brain, heart, liver, spleen, kidney, and thigh muscle) were removed 48 h after the 3rd treatment with NIR-PTT, The excised tissues were fixed with 4% buffered formalin and embedded in paraffin blocks. Tissues were sectioned into 4μm-thick sections. Hematoxylin and eosin (H&E) staining, immunostaining and immune gold-silver staining (Sigma, St. Louis, MO USA) were performed. EGFR expression in tumors and axillary LNs were investigated by immunostaining, using antibodies for EGFR (Santa Cruz Biotechnology, Dallas Texas) and an appropriate secondary antibody. Cytokeratin expression in isolated axillary LNs was investigated by immunostaining, using antibodies for Cytokeratin 8/18/19 (Abcam, Cambridge, MA, USA) and an appropriate secondary antibody. After US and PA examination, histological analyses of several organs (brain, heart, liver, spleen, kidney,

and thigh muscle) and tumors were performed. The tumors and organs of NIR-PTT were investigated by immunostaining and TUNEL staining. Immunostaining was performed using antibodies for cleaved caspase-3 (Cell Signaling Technology, Danvers, MA, USA), Ki-67 (Santa Cruz Biotechnology, Santa Cruz, CA, USA), EGFR (Cell Signaling Technology, Danvers, MA, USA) and an appropriate secondary antibody. Tissue sections were subsequently stained with counter hematoxylin solution (Millipore Ltd., Darmstadt, Germany) for 1 min. Terminal uridine deoxynucleotidyl transferase-mediated dUTP nick end labeling (TUNEL) staining with the ApopTag Peroxidase In Situ Apoptosis Detection Kit (S7100, Millipore) was used to detect apoptotic cells. Sections were stained in accordance with kit instructions and the following modifications: A 13-minute room-temperature protein digestion in prediluted proteinase K was used. Slides were incubated in equilibration buffer for 5 min, then in working strength terminal deoxynucleotidyl transferase enzyme at 37°C for 60 min, which was followed by a stop/wash step and an anti-digoxigenin peroxidase step, which were identical to kit instructions. Color development was with DAB chromogen; then, slides were counterstained with hematoxylin. Histological images of stained tissues were acquired using a microscope (Leica, Wetzlar, Germany) equipped with a CCD camera. The images were saved in TIFF format, and Image J software was used to analyze and quantify the expression of cleaved caspase-3, Ki-67 and TUNEL, and the percentage of staining was calculated.

13. Statistical analyses

For both the *in vitro* and *in vivo* data, the means ± standard deviations were calculated from at least three independent experiments and statistically evaluated using a Student-Newman-Keuls test. For all tests, *P*-values less than 0.05 were considered statistically significant.

RESULTS

***In vivo* PAI and histological analysis of axillary LNs of mice.**

Figs. 1a and 1c show representative fusion images of US B-mode and PA-mode before and after the injection of ICG and GN. The dynamics of ICG and GN uptake by the axillary LN were monitored using PAI, and the contour of the axillary LN region can be clearly seen in the fusion images of PA and US B-mode images. The mean PA signal amplitude of the axillary LNs of ICG-injected mice pre-injection was 1.60±0.30 AU, and the PA signal amplitudes at 0.5 h, 1 h, 2 h, 4 h and 24 h post-injection were 4.68±0.48 AU, 4.89±0.32 AU, 3.83±0.06 AU, 7.50±0.54 AU, 1.95±0.05 AU, respectively (Fig. 1b). A significant change in the PA signal in the axillary LN was observed at 0.5 h post-injection, indicating significant accumulation of ICG in the axillary LN regions, and was strongest 4 h after the injection of ICG (an approximately 4-fold increase relative to the pre-injection signal, $p<0.05$). The PA signal measured from the axillary LNs just before the injection was similar to that 24 h after the injection of ICG. The PA signal amplitudes in the axillary LNs of GN-injected mice pre-injection and 4 h, 12 h, 24 h, 48 h and 72 h post-injection were 2.06±0.07 AU, 3.29±0.17 AU, 6.42±0.45 AU, 9.48±0.73 AU, 11.96±0.59 AU, 9.38±0.59 AU, respectively (Fig. 1d). The PA signal amplitude in the LNs of GN-injected mice was significantly increased 4 h post-injection and reached a steady state at 48 h post-injection, indicating a maximal accumulation of GNs in the axillary LN regions (an approximately 6-fold increase relative to the pre-injection signal, $p<0.05$).

ICG-LNs were observed as dark green in color, and an obvious color change was not detected in isolated GN-LNs [Figs. 1e-f]. H&E staining showed that no histological

change was observed in ICG-LNs isolated from mice 4 h post ICG injection compared with LNs that were not injected (Fig. 1g). A large amount of accumulated GNs in the cortex and medulla area of GN-LNs isolated from mice 48 h post-injection was detected by silver staining, but there were no histological changes in the tissue as detected by H&E staining (Fig. 1h).

Assessment of selective uptake of anti-EGFR-GNs in the TNBC cell line MDA-MB-231.

The TNBC cell lines (HCC-1937 and MDA-MB-231) had high EGFR protein expression (as detected by western blot) relative to the HER2-expressing cell lines (BT474, HCC1954 and MDA-MB-453), whereas the ER-positive MCF-7 cells did not express EGFR (Fig. 2a). Silver staining showed that MDA-MB-231 cells exposed for 24 h to anti-EGFR-GNs (120 pmol/L) had a specifically and selectively higher internalization of the GNs than MCF-7 cells (Fig. 2b). Immunocytochemistry also indicated high EGFR expression in MDA-MB-231 cells (Fig. 2c). A large amount of nanoparticles in the intracellular region, mostly the endosomes/lysosomes (as indicated by the yellow arrows), was apparent in MDA-MB-231 cells treated with anti-EGFR-GNs for 24 h, whereas very few nanoparticles in the cytoplasm were observed in the MDA-MB-231 cells treated with GNs (Fig. 2d).

***In vivo* EGFR-targeted PAI and histological analysis of a xenograft tumor mouse model.**

The mean PA signal amplitudes in MDA-MB-231 tumors of anti-EGFR-GNs-injected mice pre-injection and 2 h, 4 h, 8 h, 24 h, 48 h and 72 h post-injection were 1.63±0.09 AU, 3.77±0.26 AU, 4.13±0.29 AU, 5.98±0.59 AU, 9.91±0.91 AU,

8.60±0.39 AU, 5.95±0.50 AU, respectively. The mean PA signal amplitudes in MCF-7 tumors of anti-EGFR-GNs-injected mice pre-injection and 2 h, 4 h, 8 h, 24 h, 48 h and 72 h post-injection were 1.66±0.06 AU, 2.82±0.25 AU,3.06±0.29 AU, 4.93±0.34 AU, 6.82±0.31 AU, 4.05±0.54 AU, 2.75±0.28 AU, respectively (Figs. 3a-b). The maximal value of the PA signals was reached 24 h post-injection in both groups and was significantly higher in MDA-MB-231 tumors (approximately 2-fold higher) compared with MCF-7 tumors at 48 h and 72 h post-injection ($p<0.05$). H&E staining did not show any necrotic areas in the tumors of either the MCF-7 or MDA-MB-231 group (Fig. 3c upper). MDA-MB-231 tumor tissue showed higher EGFR expression than MCF-7 tumor tissue (Fig. 3c middle). Silver staining showed a large amount of anti-EGFR-GNs accumulated in the MDA-MB-231 tumors, whereas no anti-EGFR-GNs were seen in the MCF-7 tumors (Fig. 3c lower).

However, in MCF-7 and MDA-MB-231 tumors injected with non-targeted GNs, the no significant difference in PA signals between the 2 groups at 2 h, 4 h, 24 h, 48 h and 72 h of the time points was observed (Figs. 4a-b). Non-targeted GNs, though being less accumulated in MDA-MB-231 tumors compared to anti-EGFR-GNs, can be used in *in vivo* PAI application for generally detecting tumor due to the enhanced permeability and retention (EPR) effect that is property by which non-targeted GNs tend to accumulate in tumor tissue much more that they do in normal tissues. Silver staining showed that accumulation of non-targeted GNs were not seen in the MCF-7 and MDA-MB-231 tumors at 72 h (Fig. 4c lower).

***In vivo* EGFR-targeted PAI and histological analysis of LN metastases.**

An obviously enhanced PA signal (3.67±0.18 AU) was detected in axillary LNs with metastases of MDA-MB-231-Luc tumors (n=2) at 24 h after intratumoral injection

with anti-EGFR-GNs (0.5 pmol/g mouse) compared with that of the pre-injection (1.53±0.12 AU) (Figs. 5a-c). No significant PA signal change was observed in non-metastatic axillary LNs of the MDA-MB-231-Luc tumor-bearing mice (n=4) after intratumoral injection with anti-EGFR GNs (pre vs post, 1.57±0.15 AU vs 1.61±0.13 AU) (Figs. 5b-c). *In vivo* and *ex vivo* strong bioluminescence signals were obtained in primary tumors, but no signal was detected in the axillary LNs showing the enhanced PA signals using an IVIS imaging system (Fig. 5d). As expected, H&E staining as well as EGFR and Cytokeratin 8/18/19 immunostaining of axillary LN isolated from a mouse with a strong PA signal revealed the presence of MDA-MB-231-Luc cells in the cortex and medulla area of the LN (Fig. 5e upper and middle). Silver staining and showed that the anti-EGFR-GNs injected into the tumor drained to the axillary LN harboring metastases, confirming the correlation with the increased PA signals (Fig. 5e lower). In contrast, no cancer cells and anti-EGFR-GNs were detected in those axillary LNs that showed no changes in PA signals (Fig. 5f).

Analysis of proliferation and apoptotic activity by anti-EGFR-GNs-NIR PTT in cultured MDA-MB-231 and MCF-7 cells.

The growth of MDA-MB-231 cells treated with anti-EGFR-GNs or free anti-EGFR was significantly decreased at 48 and 72 h compared with those of the untreated control (Fig. 6a; $P < 0.01$ and $P < 0.01$, respectively). Figs. 6b and 6c show the flow cytometric analysis of annexin V and propidium iodide (PI) staining on MDA-MB-231 cells after treatment with anti-EGFR-GN or free anti-EGFR for 48 h and subsequent treatment with NIR-PTT for 3 min. Irradiation with NIR light increased the culture medium up to 40°C, thereby resulting in approximately 9.34 ± 0.39% of apoptotic death of MDA-MB-231 cells ($P < 0.001$). Administration of anti-EGFR-GN or free

anti-EGFR led to 27.83 ± 0.47% or 21.27 ± 1.41% apoptotic death ($P < 0.01$). After treatment with free anti-EGFR, subsequent treatment with NIR-PTT augmented the apoptotic death (36.73 ± 2.20%, $P < 0.001$). More importantly, anti-EGFR-GN+NIR-PTT led to an increase in therapeutic temperature to 43°C, consequently resulting in the most effective apoptotic Analysis of the fundamental mechanisms of anti-proliferation and apoptosis triggered by anti-EGFR-GN combined with NIR-PTT in cultured MDA-MB-231 cells. The representative western blots and the relative analysis of HSP70, HSP90, Ki-67, cleaved caspase-3 and EGFR are shown in Figs 6d and e. The significant induction of HSP70 was the most obvious in cells treated with anti-EGFR-GN+NIR-PTT (782.13 ± 46.54 %) and anti-EGFR-GN (520.43 ± 57.93 %) (Fig. 6e; $P <0.001$). On the other hand, there is no difference in HSP90 levels in all cells. A significant decrease in proliferation marker Ki-67 was observed in cells after the treatment with anti-EGFR-GN alone (9.06 ± 1.05 %) or anti-EGFR-GN+NIR-PTT (6.18 ± 4.33 %) relative to the untreated control, whereas the significant increase in the apoptotic marker cleaved caspase-3 was observed in cells after the treatment with anti-EGFR-GN alone (259.08 ± 29.84 %) or anti-EGFR-GN+NIR-PTT (455.66 ± 70.46 %) (Fig. 6e; $P <0.001$). A significant decrease of EGFR was evident in cells treated with the anti-EGFR-GN (16.49 ± 8.03 %) and anti-EGFR-GNs+NIR-PTT (5.89 ± 2.00 %,) (Fig. 6e; $P <0.001$). Figs. 6f and 6g show the representative western blots and the relative analysis of phosphorylated mTOR, FAK, AKT and ERK1/2. When compared with those of untreated control, the decrease of phosphorylated mTOR in NIR-PTT alone, anti-EGFR-GNs alone and anti-EGFR-GN+NIR-PTT was 61.25 ± 15.22 %, 21.84 ± 8.21 %, and 8.51 ± 1.92 %, respectively (Fig. 6g; $P < 0.01$ or $P< 0.001$). The phosphorylated FAK decreased up to 50.14 ± 3.79 %, 17.67 ± 5.83 %, and 7.67± 1.51 % in NIR-PTT alone, anti-EGFR-GN alone and anti-EGFR-GN+NIR-PTT, respectively,

relative to that of untreated control (Fig. 6g; $P < 0.001$). Phosphorylated AKT in cells treated with NIR-PTT alone, anti-EGFR-GN alone and anti-EGFR-GN+NIR-PTT relative to untreated control was decreased by 93.24 ± 12.26 %, 18.83 ± 2.18 %, and 11.50 ± 4.81 %, respectively (Fig. 6g; $P < 0.001$). Phosphorylated ERK1/2 treated by NIR-PTT alone, anti-EGFR-GN alone and anti-EGFR-GN+NIR-PTT was also significantly decreased by 59.46 ± 6.67 %, 23.04 ± 7.70%, and 6.37 ± 2.18 %, respectively, compared with those of the untreated control (Fig. 6g; $P < 0.001$). Anti-EGFR-GN combined with NIR-PTT resulted in synergistic promotion of anti-proliferative and apoptotic signals and was more effective for suppressing the phosphorylation of mTOR, FAK, AKT and ERK1/2 compared to those of NIR-PTT alone or anti-EGFR-GN alone (42.61 ± 0.95%, $P < 0.001$).

The treatment with anti-EGFR or anti-EGFR-GN did not affect the growth in MCF-7 cells, which do not express EGFR (Fig. 7a). The treatment with anti-EGFR or anti-EGFR-GN did not cause death of MCF-7 cells, but NIR-PTT did cause apoptotic death (12.23 ± 0.31%). The anti-EGFR-GN+NIR-PTT did not augment apoptotic death of MCF-7 cells (Figs. 7 b-c). Our results revealed that anti-EGFR-GN combined with NIR-PTT worked by selectively and synergistically inducing anti-proliferation and apoptosis in MDA-MB-231 cells but not in MCF-7 cells.

***In vivo* US-guided PAI and BLI to monitor the therapeutic response in xenograft tumor models during treatment with anti-EGFR-GN combined with NIR-PTT.**

Fig. 8a shows the therapy strategy for xenograft tumors. When the tumors reached a volume of 150-200 mm^3 at 2 weeks, NIR-PTT was performed at 48 h after the three intravenous injections of anti-EGFR-GNs at 4-day intervals because anti-EGFR-GNs were specifically and maximally accumulated into MDA-MB-231 tumors at between

24 h and 48 h and tumors was monitored by longitudinal follow-up US-guided PAI and BLI. Fig. 8b shows representative color Doppler images and US-guided PAIs obtained from tumors in each group. Treatment with anti-EGFR, anti-EGFR-GN and anti-EGFR-GN+NIT-PTT did not cause significant differences in the body weights of mice after three trails, and the damage of normal tissues compared to those of untreated mice, suggesting the absence of physical distress over the course of the experiment. As shown in Fig. 8c, enhanced PA signal amplitudes in tumors of control and anti-EGFR-injection mice were not observed, yet greatly enhanced PA signals in tumors were evident in anti-EGFR-GN-injected mice, indicating the selective accumulation of anti-EGFR-GNs into the tumor mass. The mean PA signal amplitude of tumors was approximately 9.18 ± 0.56 to 10.00 ± 0.71 AU at 48 h after first injection with anti-EGFR-GNs but gradually decreased after two and three treatments with anti-EGFR-GN (8.46 ± 0.30, 6.52 ± 0.19 AU) or anti-EGFR-GN+NIR-PTT (3.21 ± 0.1, 1.24 ± 0.08 AU), which may selectively reflect EGFR-positive tumor cell damage or tumor vascular insult during therapeutic intervention in tumors with the anti-EGFR or NIR-PTT.

Figs. 9a and 9b show representative BLI of tumors and the quantification of the photon flux measured from tumors in each group. An obvious decrease of photonic flux of tumors at the indicated times after the 1st, 2nd and 3rd treatment with anti-EGFR (0.64 ± 0.26, 0.84 ± 0.13 and 0.15 ± 0.11 photons/s/cm^2/sr), anti-EGFR-GN (1.40 ± 0.24, 0.23 ± 0.29 and 0.08 ± 0.03 photons/s/cm^2/sr) and anti-EGFR-GN+NIR-PTT (0.22 ± 0.41, 0.07 ± 0.11 and 0.04 ± 0.04 photons/s/cm^2/sr) was observed compared with those of untreated controls (1.20 ± 0.42, 1.10 ± 0.28 and , 1.95 ± 0.17 photons/s/cm^2/sr), respectively (Fig. 9b; $P < 0.001$). Bioluminescence activity in tumors during the 2nd and 3rd treatments with anti-EGFR-GN+NIR-PTT almost

disappeared, which indicates that most tumor cells are not viable. A significantly continuous decrease of tumor volumes was observed in the anti-EGFR-treated mice (137.30 ± 10.42 mm^3), anti-EGFR-GN-treated mice (117.72 ± 22.19 mm^3) and anti-EGFR-GN+NIR-PTT-treated mice (21.94 ± 9.41 mm^3) during the third post-treatment compared to those of control mice (254.48 ± 10.60 mm^3), whereas tumor volumes of the control group continued to increase gradually (Fig. 9c; $P < 0.001$). The anti-EGFR-GN combined with NIR-PTT showing strong therapeutic effects is most encouraging, resulting in successful tumor regression *in vivo* at the third post-treatment compared to that of the initial tumor volume.

Histological analysis of tumor tissues treated with anti-EGFR-GN combined with NIR-PTT.

The gross images of tumor tissues revealed the smallest residual tumor volume in anti-EGFR-GN+NIR-PTT groups (Fig. 10a). From analysis of H&E images, the necrotic area in residual tumor tissues of the anti-EGFR-GN+NIR-PTT group was not observed (Fig. 10b). Consistent with the *in vitro* results of cultured cells assessed by western blot analysis, representative immunohistochemical images showed higher cleaved caspase-3 and TUNEL staining as well as lower Ki-67 and EGFR staining in the anti-EGFR-GN+NIR-PTT tumors than in the other tumors (Fig. 10c). TUNEL staining was significantly higher in the anti-EGFR-GN tumors (1.93 ± 0.42%) and anti-EGFR-GN+PTT tumors (5.2 ± 0.66%) but not in anti-EGFR tumors (0.67 ± 0.15%) relative to control tumor (0.67 ± 0.25%) (Fig. 10d; $P < 0.001$). Cleaved caspase-3 staining was also significantly higher in tumors treated with anti-EGFR (21.0 ±3.61%), anti-EGFR-GN (44.33 ± 5.86%) and anti-EGFR-GN+NIR-PTT (73.33 ± 10.69%) relative to control (14.0 ± 3.61%) (Fig. 10e; $P < 0.001$). On the contrary, Ki-67 staining

was significantly lower in the anti-EGFR (18 ± 3.0%), anti-EGFR-GNs (8.67 ± 2.08%) and anti-EGFR-GN+NIR-PTT tumors (3.66 ± 1.52%) compared to that in control cells (30 ± 5.0%) (Fig. 10f; $P < 0.001$). In addition, EGFR staining was significantly lower in the anti-EGFR (3.4 ± 0.75%), anti-EGFR-GN (1.33 ± 0.20%) and anti-EGFR-GN+NIR-PTT tumors (0.83 ± 0.35%) compared with that in control tumor (17±4.0%) (Fig. 10g; $P < 0.001$). Histological analysis revealed that anti-EGFR-GN combined with NIR-PTT eventually led to the most effective therapy for tumor regression through augmentation of the synergic mechanisms of anti-proliferation and apoptosis. From analysis of H&E staining, we did not observe damage or histological alteration of the liver, spleen or kidney of each group (Fig 10h). In the silver staining, even though accumulated anti-EGFR-GNs were not detected in liver and spleen, a few remained in the kidney at 4 days after the third post-treatment of anti-EGFR-GNs (Fig. 10h).

DISCUSSION

PAI using various exogenous contrast agents (methylene blue, ICG and GNs) is a rapidly emerging non-ionizing and noninvasive imaging technology that integrates the merits of strong optical contrast with high spatial resolution to image the course and flow of lymphatic vessels as well as to selectively detect breast tumors, including metastases [10-13]. PAI easily integrates the clinical US imaging system and has shown tremendous potential in accurately detecting primary tumor and LN metastases while simultaneously providing structural, functional and molecular information at clinically relevant penetration depths [10]. Because breast cancer cells often invade regional LN receiving the drainage from a tumor, accurate detection of regional LN metastases can help to determine the stage of the breast cancer and develop an appropriate treatment plan for the breast cancer patient [18, 32-34]. Moreover, a sentinel node biopsy guided by ICG or PAI can avoid postoperative complications, such as seroma formation, lymphedema, and limited motion, of an axillary LN dissection [35, 36]. In an effort to improve on accurate identification and safe dissection of metastatic LNs, non-invasive imaging modalities including bioluminescence imaging, positron emission tomography (PET), US and magnetic resonance imaging (MRI) have been tested in animal models and patients but currently lack the specificity and sensitivity to discriminate between metastatic and normal LNs. Our results showed that non-invasive EGFR-targeted US-guided PAI is sensitive enough to detect the primary tumor and metastatic LNs in a mouse model of human TNBC.

Multifunctional contrast agents loaded with specific antibodies and therapeutic drugs have been suggested to improve the delivery limitations, such as enzymatic

degradation, inadequate pharmacokinetics and tissue accessibility, of therapeutic antibodies and drugs, thereby reducing non-specific side effects and enabling higher dose delivery to target tissues over expressing the cell surface receptor [10, 15]. Rod-shape gold nanoparticles characterized by enhanced optical absorption and photostability are attractive PA contrast agents because of their production of strong PA signals as well as their ability to conjugate biomolecules to them for PAI. In the present study, we highlighted the potential of using PAI combined with intravenous anti-EGFR-GNs (0.5 pmol/g mouse) injections to selectively visualize EGFR-expressing breast cancer cells. In our study, the intravenously injected GN concentration is lower than previously reported doses [16, 37]. Moreover, the amount of anti-EGFR antibody (0.92 μg/g animal) loaded in the GNs was lower compared with a clinical trial using cetuximab [6] but was a sufficient amount for specific and selective targeting of EGFR-expressing cancer cells. The maximum accumulation of all tested nanoparticles after intravenous injection occurred in the liver and spleen. In agreement with most published reports [16], the very small amount of GNs accumulated in the liver and spleen was detected by silver staining.

Luke GP *et. al.* showed the *in vivo* application of PAI to non-invasively detect the LN micrometastases (<50μm) using intratumoral injection with 1.6 pmol of spherical gold nanoparticles targeted to the EGFR oral cancer animal models, but the LN micrometastatic foci (<50μm) was able to detected by using bioluminescence imaging method [13]. Very recently, although the functional spectroscopic PAI to measure the blood oxygen saturation in the LN led to less sensitivity and specificity to discriminate metastatic LN as compared to PAI using exogenous PA contrast agents, this approach might open up the suitable possibility for clinical applications[38]. Recently, TNBC was subclassified to a very heterogeneous subtype based on gene expression analysis;

translational and clinical studies for emerging targeted TNBC therapies have therefore been facilitated by increased understanding of the aberrant gene expression regulating growth and survival [4, 5]. EGFR, which is detected to be highly expressed in 70% of TNBCs, has represented a clinically relevant molecular target for TNBC patients [9, 39]. The anti-EGFR antibodies bind to EGFR, thereby blocking its downstream signaling through its internalization and degradation, and can lead to cytotoxicity [40]. Many clinical Phase I/II investigations for TNBC patients have tried using FDA-approved anti-EGFR antibody Cetuximab combined with chemotherapy [6, 7, 9, 41], yet the results have been somewhat disappointing.

In our study, PAI by intratumoral injection of 0.5 pmol/g mouse anti-EGFR-GNs, which is a significantly lower amount compared with that of previous reports [42] clearly identified small colonies of EGFR-expressing cancer cells that spread to the axillary LNs, even though bioluminescence imaging technology did not detect the cancer cell in LNs. Our result showed that anti-EGFR-GNs-enhanced PAI is more sensitive than bioluminescence imaging for the early detection of breast cancer cells that have migrated to regional LNs. Our studies combining US-guided PAI with anti-EGFR-GNs may be able to achieve simultaneous sensitivity and specificity values approaching 100% to discriminate LN micrometastases from normal LN.

The anticancer therapy of multifunctional GNs loaded with cetuximab and a low dose of gemcitabine in an orthotopic pancreatic cancer model was superior to that of the antibody alone, drug alone or combination of the two [42], suggesting that anti-EGFR-GNs can be used for treating EGFR-expressing breast cancer cell LN metastases. Although the concentration of anti-EGFR-GNs in this study is below the previously reported amount exhibiting toxicity, GNs are not yet accepted for widespread clinical use. Further studies regarding the pharmacokinetics, biodistribution and *in vivo* toxicity

of anti-EGFR-GNs used as a clinical therapy need to be conducted because particles larger than 5 to 6 nm are not easily cleared from the body [16]. Our results suggest that non-invasive EGFR-targeted PAI is a relevant approach for use in the clinic to improve the selective and effective targeted delivery of chemotherapeutics into EGFR-expressing tumors and to guide real-time surgery of LN micrometastases and residual tumors with EGFR-expressing cancer cells, following some alterations in the system to make it functional and safe for humans.

In the present study, we have proven an improvement in the therapeutic efficacy of anti-EGFR antibody treatment by intravenous injection with GNs to effectively delivery anti-EGFR antibodies into TNBCs, which showed strong inhibition of the EGFR-mediated signaling pathway and apoptotic cell death. Most importantly, the anti-EGFR-GNs combined with NIR-PTT strategy exhibited the most successful therapeutic efficacy by selectively targeting TNBC cells and tumors without any damage to normal tissues through the augmented mechanism of anti-proliferative and apoptotic activity.

PTT is a noninvasive cancer therapy technique that promotes tumor destruction by altering the function of many structural and enzymatic proteins within cancer cells, thereby leading to successful destruction of the cancer cells [43, 44]. Considerable research is being directed towards developing nanoparticles, including GNs, for a wide range of biomedical applications, such as molecular diagnosis and targeted therapy via site-specific targeted delivery and stabilizing labile molecules including antibodies from degradation [15, 16, 22]. GNs have been brought to the forefront of cancer research in recent years because of their convenient synthesis and surface modifications for specific molecular delivery as well as tunable optical properties for PAI applications and NIR-PTT [10, 16, 22, 45, 46]. GNs with optical absorption in the

NIR spectrum (700−1000 nm), which is the most advantageous wavelength region suitable for biological applications owing to its high capability of deeper penetration into animal tissues in this optical window, have recently been developed and successfully applied with NIR-PTT to cause damage to localized primary and metastatic cancer [19, 23, 46]. Anti-EGFR-GNs with a desired optical absorption in the NIR spectrum (808 nm) have unique properties that provide the potential for simultaneously selectively targeting PAI and NIR-PTT applications *in vivo*. However, to the best of our knowledge, NIR-PTT using anti-EGFR-GNs has not yet been applied to TNBCs *in vitro* and *in vivo*. Moreover, the detailed biological mechanisms of cellular therapeutic response to anti-EGFR-GNs combined with NIR-PTT have not been explored.

In our study, TEM images revealed that a large amount of anti-EGFR-GNs are taken up by MDA-MB-231 cells, resulting in the accumulation in endosomes or lysosomes, consistent with many studies with regards to nanoparticles being endocytosed by cells, particularly when attached to a receptor ligand such as an internalized antibody, and accumulate in endosomes or lysosomes [16]. We found here that significant uptake of anti-EGFR-GNs suppressed the proliferation activity of MDA-MB-231 cells compared to that with non-targeted GNs, which is involved in blocking EGFR-mediated signaling molecules (mTOR, AKT, FAK and ERK) and suppressing EGFR and Ki-67 through the selective and effective delivery of the anti-EGFR-antibodies. The possible modes of cell death triggered by PTT include necrosis and apoptosis. More specifically, high-energy irradiation can lead to necrosis and low-energy irradiation can promote apoptosis. In our conditions, with exposure to NIR light, anti-EGFR-GNs induced mild hyperthermia, defined in cancer treatment as a rise in tissue temperature to 40–43 °C, which implies anti-EGFR-GNs are effective

photothermal agents. More importantly, we demonstrated that anti-EGFR-GNs combined with NIR-PTT induced an increase in HSP70 and cleaved caspase-3, augmented the blockade of the phosphorylation of mTOR, AKT, FAK and ERK and the suppression of EGFR and Ki-67 in cultured MDA-MB-231 cells, which suggesting the molecular mechanism of synergistic apoptotic and anti-proliferative activity, not necrosis, is involved in tumor cell death. Taken together in an *in vitro* study, PTT combined with NIR light and anti-EGFR-GNs has proven to be a selective and effective therapy in TNBC cell lines expressing EGFR. Anti-EGFR-GNs combined with NIR-PTT, resulting from *in vitro* studies, offers a favorable therapeutic strategy for EGFR-expressing TNBC tumors.

Anti-EGFR-GNs, resulting from the regression of tumor volumes in xenograft mice models, enhanced the therapeutic effect compared with that of free anti-EGFR antibodies, thus offering the feasibility of an excellent nanoplatform for *in vivo* therapy applications. One of the most promising directions in PTT is the use of GNs with peak transmission at approximately 800 nm and 10 to 100 nm in diameter because skin, tissues, and hemoglobin have transmission windows from 650 to 900 nm, and the bloodstream circulation times of GNs are increased, which causes improved tumor accumulation from an intravenous administration and leads to better effects of PTT [10, 17, 23, 46]. We speculate that anti-EGFR-GNs are excellent for NIR-PTT applications *in vivo* due to their properties of peak absorbance at 808 nm and long circulation time. As we expected, anti-EGFR-GNs combined with NIR-PTT led to remarkably greater tumor regression compared with treatment with either anti-EGFR antibody injection alone or anti-EGFR-GNs injection alone, significantly reducing proliferation activity (low Ki-67 level) and inducing apoptotic activity (high cleaved caspase-3 and TUNEL-positive levels) in sections of the MDA-MB-231 tumors.

In conclusion, US-guided PAI technology using anti-EGFR-GNs is feasible and highly sensitive. It allows for the selective visualization of EGFR-targeted primary tumors as well as LN micrometastases in a murine model of human TNBC. Our study demonstrates that anti-EGFR-GNs are feasible diagnosis and therapy agents for simultaneously applying selective EGFR-targeted PAI and NIR-PTT to aggressive EGFR-positive cancers due to their properties of selective tumor cell targeting, long circulation time and desired optical absorption upon NIR irradiation light. By the exposure of EGFR-positive TNBC cells and tumors treated with anti-EGFR-GNs to NIR light, blockade of the EGFR-mediated intracellular signal pathway (low phosphorylated mTOR, AKT, ERK and FAK levels) involved in cell proliferation and survival as well as the strong anti-proliferative (low Ki-67 level) and apoptotic activity (high cleaved caspase-3 and TUNEL staining levels) of tumor cells and tumor tissues were observed. Anti-EGFR-GNs represent reliable and reproducible photothermal agents on favorable NIR lights. Anti-EGFR-GNs combined with NIR-PTT is a feasible and effective therapeutic strategy, which enables selective tumor cell targeting through the synergistic mechanism of anti-proliferation and apoptosis without side effects and complications compared with previous conventional therapy strategy. US-guided PAI and anti-EGFR-GNs combined with NIR-PTT would be a novel theranostic system to simultaneously investigate non-invasive and longitudinal diagnosis and therapy of EGFR-positive TNBC in experimental studies.

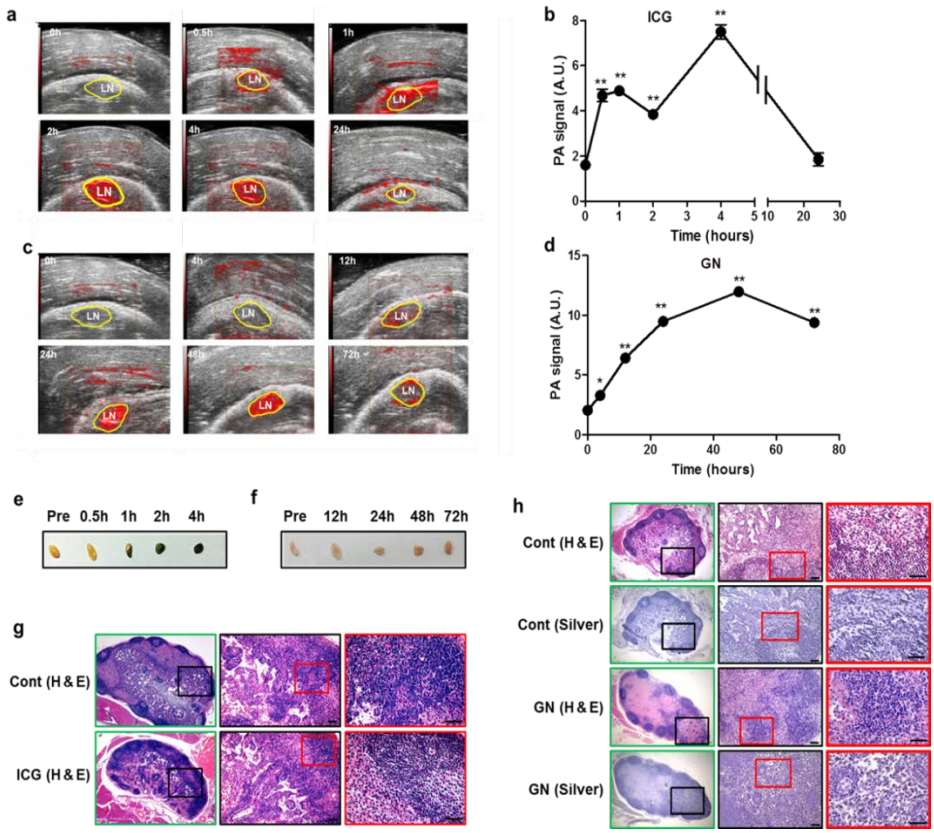

Figure 1： Analysis of US-guided photoacoustic (PA) images and histology of the axillary LN of mice injected with ICG or gold nanorods (GN). (a) Non-invasive and dynamic fusion of US and PA images of the axillary LN region before and 0.5 h, 1 h, 2 h, 4 h and 24 h after ICG injection (5 pmol/g mouse). (b) Plot of PA signal amplitude in axillary LNs versus pre- and post-injection time of ICG. (c) Non-invasive and dynamical fusion of US and PA images of axillary LN region before and 4 h, 12 h, 24 h, 48 h and 72 h after GN injection (0.005 pmol/g mouse). (d) Plot of PA signal amplitude in axillary LNs versus pre- and post-injection time of GN. The results represent the mean±standard deviation in the ICG-mice group (n=5) and the GN-mice group (n=5), *p<0.05, **p<0.01, Arbitrary units (AU). (e, f) Photographs of isolated axillary LN before and after injection of ICG or GN. (g) H&E staining of microsectioned axillary LN isolated from mice 4 h post-injection of ICG. (h) H&E staining and silver staining of microsectioned axillary LN isolated from mice at 48 h post-injection of GN. The control (Cont) is a microsectioned axillary LN without injection of ICG or GN. Scale bar: 100 μm.

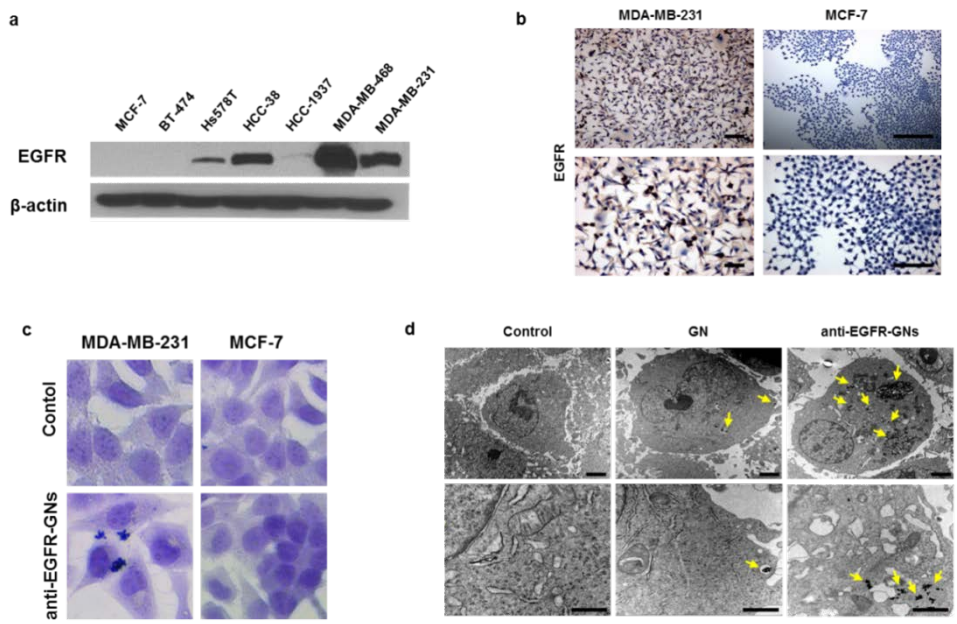

Figure 2. Analysis of EGFR expression and selective uptake of anti-EGFR-GNs in breast cancer cells. (a) EGFR expression in MCF-7, BT-474, Hs578T, HCC-38, HCC-1937, MDA-MB-453 and MDA-MB-231 human breast cancer cell lines (by western blot). (b) Representative immunocytochemistry for EGFR in MDA-MB-231 cells and MCF-7 cells. (c) Silver staining of MCF-7 and MDA-MB-231 cells incubated with or without 120 pmol/L of anti-EGFR-GNs for 24 h. Control (Cont) was incubated without 120pmol/L of anti-EGFR-GNs. (d) TEM images of MDA-MB-231 cells treated with GNs or anti-EGFR-GNs for 24 h. TEM images revealed a large amount of endocytic uptake of anti-EGFR-GNs (yellow arrows) by MDA-MB-231 cells. Scale bar: 1 μm.

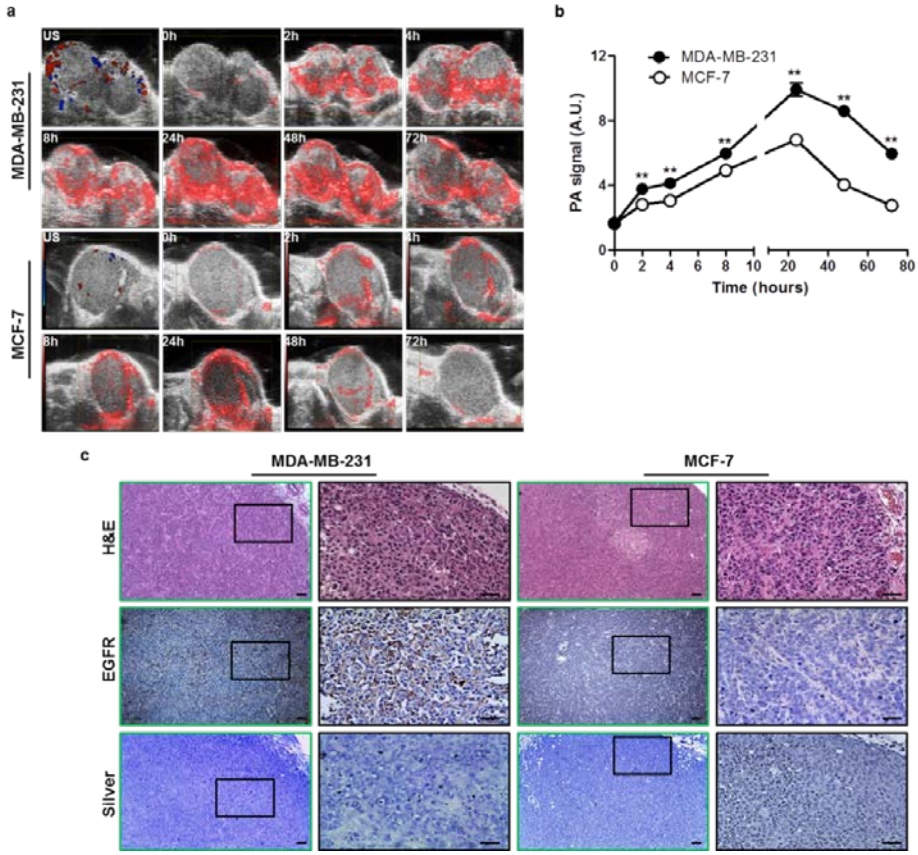

Figure 3. US-guided PAI and histology acquired in MCF-7 and MDA-MB-231 primary tumors of mice intravenously injected with anti-EGFR-GNs. (a) Non-invasive and dynamical fusion of US and PA images of MCF-7 and MDA-MB-231 tumors before and 2 h, 4 h, 8 h, 24 h, 48 h and 72 h after intravenous injection with anti-EGFR-GNs (0.5 pmol/g mouse). (b) Plot of PA signal amplitude in MCF-7 and MDA-MB-231 tumors versus pre- and post-injection of anti-EGFR-GNs. The results represent the mean±standard deviation in the MCF-7-mice group (n=5) and MDA-MB-231-mice group (n=5). **p<0.01, Arbitrary units (AU). (c) H&E staining, EGFR immunostaining and silver staining of microsectioned MDA-MB-231 and MCF-7 primary tumors isolated from mice 48 h post-injection of anti-EGFR GN. Scale bar: 100 μm.

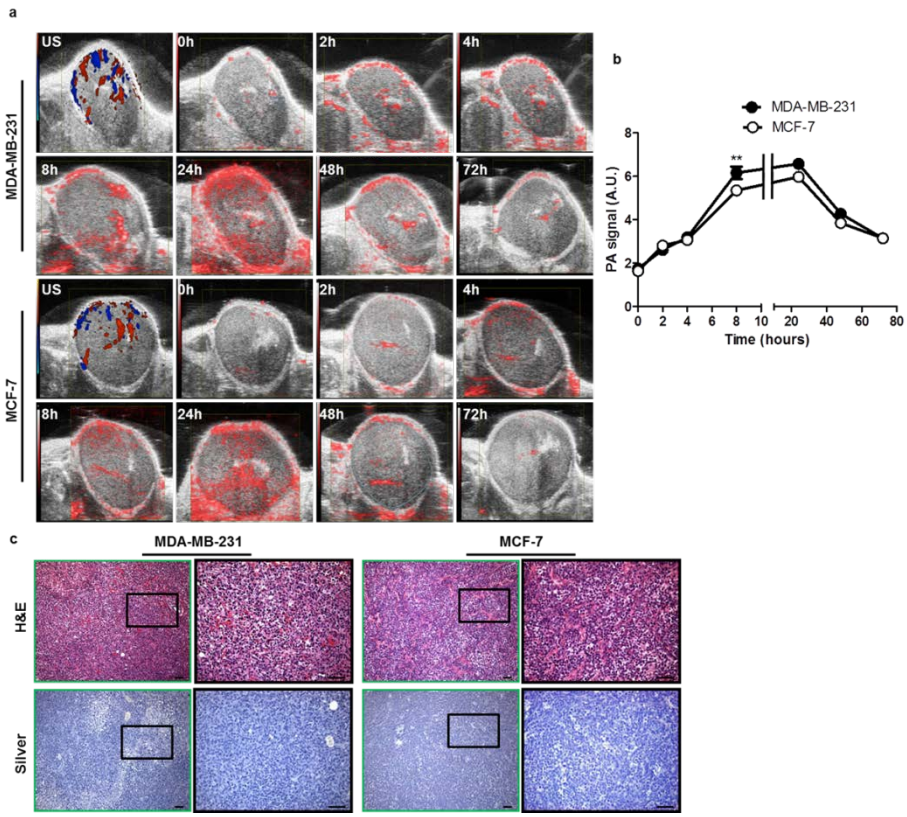

Figure 4. US-guided PAI and histology acquired in MCF-7 and MDA-MB-231 primary tumors of mice intravenously injected with GNs. (a) Non-invasive and dynamical fusion of US and PA images of MCF-7 and MDA-MB-231 tumors before and 2 h, 4 h, 8 h, 24 h, 48 h and 72 h after intravenous injection with non-targeted GNs (0.5pmol/g mouse). (b) Plot of PA signal amplitude in MCF-7 and MDA-MB-231 tumors versus pre-and post-injection of non-targeted GNs. The results represented the mean±standard deviation in the MCF-7-mice group (n=5) and MDA-MB-231-mice group (n=5). **p<0.01, Arbitrary units (AU). (c) H&E staining and silver staining of microsectioned MDA-MB-231 and MCF-7 primary tumor isolated from mice 48 h post-injection of non-targeted GNs. Scale bar: 100 μm.

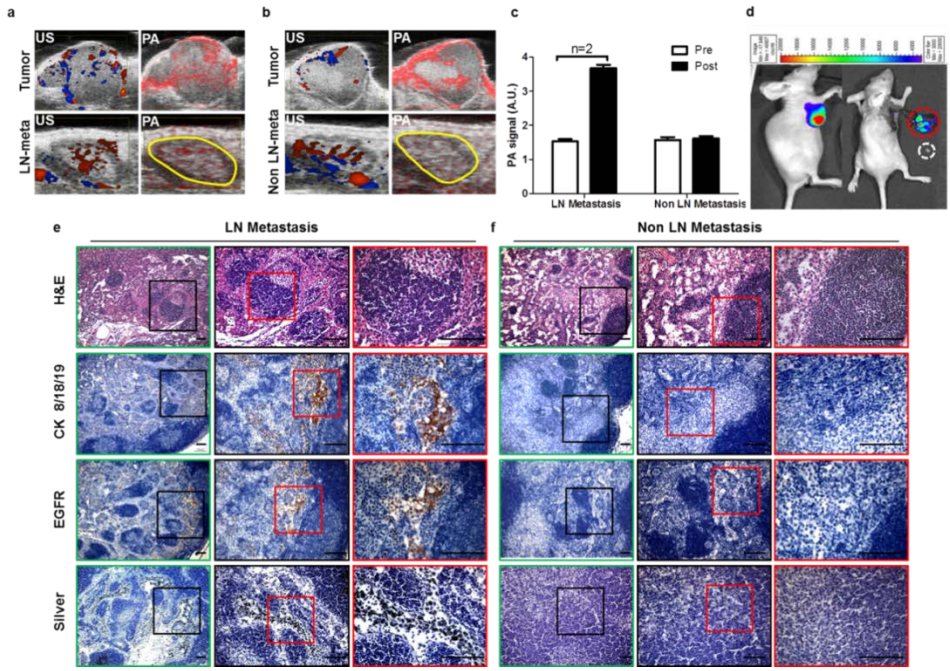

Figure 5. ***In vivo*** **EGFR-targeted PAI and histological analysis of LN metastases** (a, b) Non-invasive and dynamical fusion of US and PA images of axillary LN metastases and non-LN metastases in MDA-MB-231-Luc tumor-bearing mice 24 h after intratumoral injection with anti-EGFR-GNs (0.5 pmol/g mouse). (c) Plot of PA signal amplitude in axillary LN at pre- and post-injection of anti-EGFR-GNs. The results represent the mean±standard deviation in the LN metastases mice group (n=2) and non-LN metastases mice group (n=4), Arbitrary units (AU). (d) *In vivo* (left) and *ex vivo* (right) bioluminescence imaging of MDA-MB-231-Luc tumor-bearing mice injected intraperitoneally with D-luciferin (150 μg/g mouse). Red and white circles indicate the excised primary tumor and axillary LN from *ex vivo* bioluminescence imaging. (e, f) H&E staining, EGFR and cytokeratin 8/18/19 immunostaining and silver staining of microsectioned axillary LNs isolated from mice at 48 h post-injection of anti-EGFR GNs. Scale bar: 100 μm.

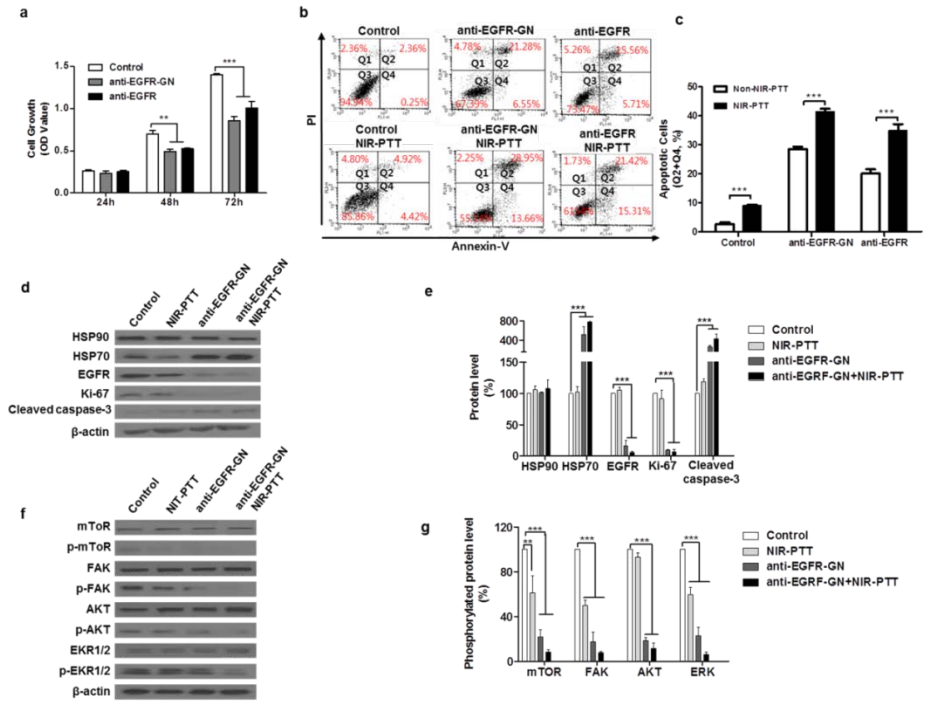

Figure 6. Analysis of cell proliferative and apoptotic action caused by anti-EGFR-GN combined NIR-PTT in cultured MDA-MB-231 cells. (a) Analysis of cell growth (mean±S.D., n=5) assessed by MTT assay in MDA-MB-231 cells treated with anti-EGFR-GNs (120 pM) and anti-EGFR antibodies (0.22 μg/ml) for 24, 48 and 72 h. (b) Representative flow cytometric analysis of Annexin V and PI MDA-MB-231 cells treated with anti-EGFR-GNs (120 pM) and anti-EGFR antibodies (0.22 μg/ml) for 24 h and combined NIR-PTT for 3 min. (c) Analysis of apoptotic cell death (mean±S.D., n=4) assessed by flow cytometry. (d, f) Representative western blot of heat shock proteins (HSP90, HSP70), EGFR, Ki-67, cleaved caspase-3 and EGFR-mediated intracellular signaling molecules (mTOR, FAK, AKT, ERK1/2) in MDA-MB-231 cells treated with NIR-PTT, anti-EGFR-GNs and anti-EGFR-GNs combined with NIR-PTT. (e, g) Data (mean±S.D., n=5) were obtained from western blot experiments. $^{**}P < 0.01$, $^{***}P < 0.001$.

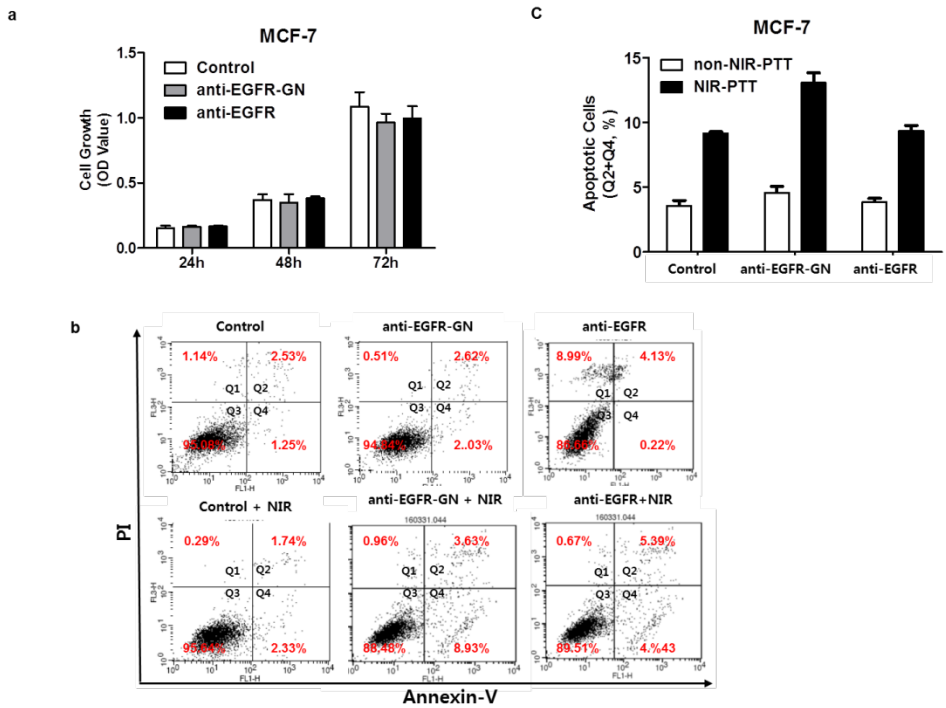

Figure 7. Analysis of cell proliferative and apoptotic action caused by anti-EGFR-GN combined NIR-PTT in cultured MCF-7 cells. (a) Analysis of cell growth (mean±S.D., n=5) assessed by MTT assay in MCF-7 cells treated with anti-EGFR-GNs (120 pM) and anti-EGFR antibodies (0.22 μg/ml) for 24, 48 and 72 h. (b) Representative flow cytometric analysis of Annexin V and PI in MCF-7 cells treated with anti-EGFR-GNs (120 pM) and anti-EGFR antibodies (0.22 μg/ml) for 24 h and combined NIR-PTT for 3 min. (c) Analysis of apoptotic cell death (mean±S.D., n=4) assessed by flow cytometry. $^{**}P < 0.01$, $^{***}P < 0.001$.

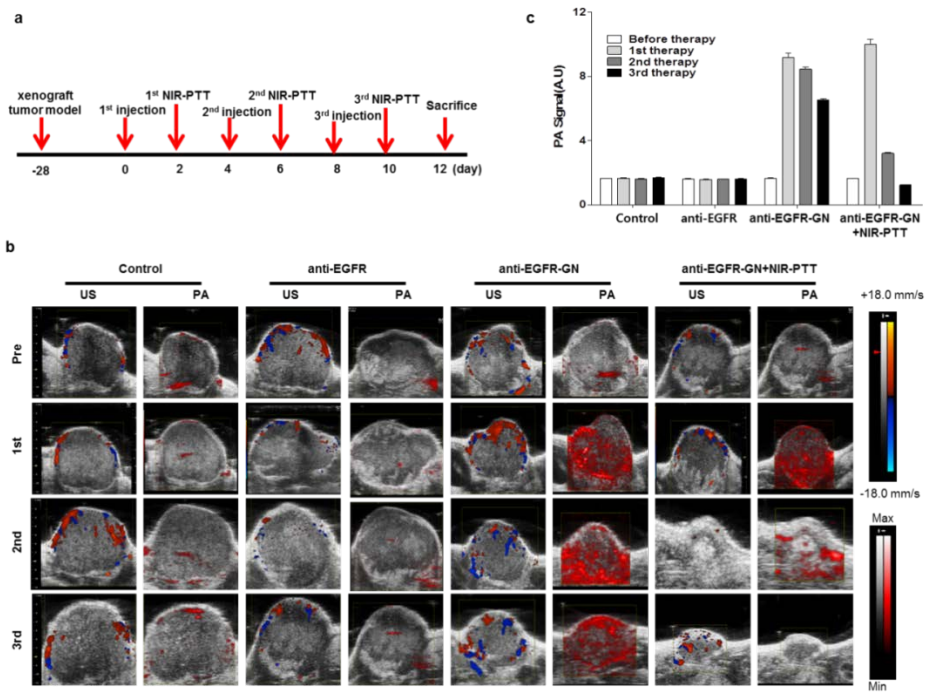

Figure 8. Analysis of PAI-guided NIR-PTT using anti-EGFR-GN combined in xenograft tumors. (a) Scheme for the *in vivo* experimental procedure. (b) Representative serial US-guided PAI of tumors in mice receiving 2nd and 3rd EGFR-GNs combined with NIR-PTT treatments. Left and right images show 2D color Doppler images and PAI superimposed on the B-mode real-time US in each group. (c) PA signals (mean±S.D.) were measured from 5 tumors of each group at pre-, and 1st, 2nd and 3rd treatments. ***P* < 0.01, ****P* < 0.001.

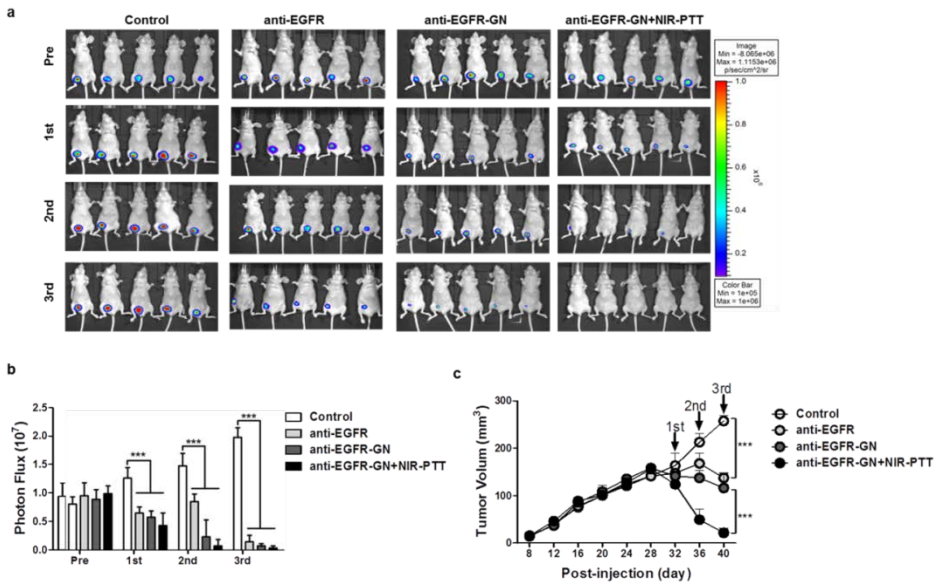

Figure 9. Analysis of bioluminescence imaging (BLI) to monitor the therapeutic response in xenograft tumor models during treatment. (a) Representative non-invasive bioluminescence imaging in tumors of each mouse group. (b) Photon flux (mean±S.D.) was measured from 5 tumors of each group at pre-, 1st, 2nd and 3rd treatments. (c) Tumor volumes (mean±S.D.) were measured from 5 tumors of each group. $^{**}P < 0.01$, $^{***}P < 0.001$.

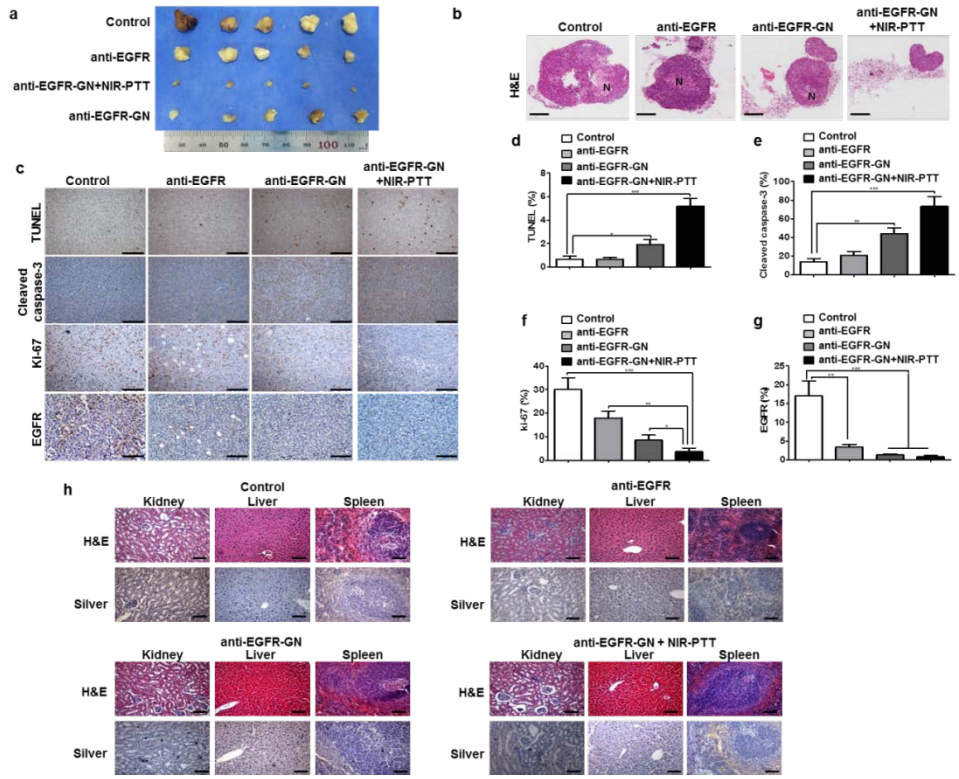

Figure 10. **Histological analysis of tumor tissues treated with anti-EGFR-GN combined with NIR-PTT.** (a) Gross images of the tumors isolated from each mouse group. (b) Representative H&E images of the tumors isolated from each mouse group. Necrotic areas (N) in residual tumor tissues. (c) Representative immunohistochemistry images of TUNEL, cleaved caspase-3, Ki-67 and EGFR staining. (d e, f, g) TUNEL-, cleaved caspase-3-, Ki-67- and EGFR-positive populations (mean±S.D.) were analyzed from 5 tumor sections of each group. (h) H&E and silver staining of kidney, liver and spleen tissues isolated from each mouse group. Scale bar: 100 μm.. $^{**}P < 0.01$, $^{***}P < 0.001$.

REFERENCES

1. Wu, J.M., Fackler, M.J., Halushka, M.K., Molavi, D.W., Taylor, M.E., Teo, W.W., Griffin, C., Fetting, J., Davidson, N.E., De Marzo, A.M., et al. (2008). Heterogeneity of breast cancer metastases: comparison of therapeutic target expression and promoter methylation between primary tumors and their multifocal metastases. Clinical cancer research : an official journal of the American Association for Cancer Research *14*, 1938-1946.
2. Kaufmann, M., Pusztai, L., and Biedenkopf Expert Panel, M. (2011). Use of standard markers and incorporation of molecular markers into breast cancer therapy: Consensus recommendations from an International Expert Panel. Cancer *117*, 1575-1582.
3. Goldhirsch, A., Wood, W.C., Coates, A.S., Gelber, R.D., Thurlimann, B., Senn, H.J., and Panel, m. (2011). Strategies for subtypes--dealing with the diversity of breast cancer: highlights of the St. Gallen International Expert Consensus on the Primary Therapy of Early Breast Cancer 2011. Annals of oncology : official journal of the European Society for Medical Oncology / ESMO *22*, 1736-1747.
4. Crown, J., O'Shaughnessy, J., and Gullo, G. (2012). Emerging targeted therapies in triple-negative breast cancer. Annals of oncology : official journal of the European Society for Medical Oncology / ESMO *23 Suppl 6*, vi56-65.
5. Lehmann, B.D., Bauer, J.A., Chen, X., Sanders, M.E., Chakravarthy, A.B., Shyr, Y., and Pietenpol, J.A. (2011). Identification of human triple-negative breast cancer subtypes and preclinical models for selection of targeted therapies. The Journal of clinical investigation *121*, 2750-2767.
6. Carey, L.A., Rugo, H.S., Marcom, P.K., Mayer, E.L., Esteva, F.J., Ma, C.X., Liu, M.C., Storniolo, A.M., Rimawi, M.F., Forero-Torres, A., et al. (2012). TBCRC 001: randomized phase II study of cetuximab in combination with carboplatin in stage IV triple-negative breast cancer. Journal of clinical oncology : official journal of the American Society of Clinical Oncology *30*, 2615-2623.
7. Ferraro, D.A., Gaborit, N., Maron, R., Cohen-Dvashi, H., Porat, Z., Pareja, F., Lavi, S., Lindzen, M., Ben-Chetrit, N., Sela, M., et al. (2013). Inhibition of triple-negative breast cancer models by combinations of antibodies to EGFR. Proceedings of the National Academy of Sciences of the United States of America *110*, 1815-1820.
8. Graham, J., Muhsin, M., and Kirkpatrick, P. (2004). Cetuximab. Nature reviews. Drug discovery *3*, 549-550.
9. Baselga, J., and Arteaga, C.L. (2005). Critical update and emerging trends in epidermal growth factor receptor targeting in cancer. Journal of clinical oncology : official journal of the American Society of Clinical Oncology *23*, 2445-2459.
10. Wang, L.V., and Hu, S. (2012). Photoacoustic tomography: in vivo imaging from organelles to organs. Science *335*, 1458-1462.
11. Eghtedari, M., Oraevsky, A., Copland, J.A., Kotov, N.A., Conjusteau, A., and Motamedi, M. (2007). High sensitivity of in vivo detection of gold nanorods using a laser optoacoustic imaging system. Nano letters *7*, 1914-1918.

12. Luke, G.P., Yeager, D., and Emelianov, S.Y. (2012). Biomedical applications of photoacoustic imaging with exogenous contrast agents. Ann Biomed Eng *40*, 422-437.
13. Siphanto, R.I., Thumma, K.K., Kolkman, R.G., van Leeuwen, T.G., de Mul, F.F., van Neck, J.W., van Adrichem, L.N., and Steenbergen, W. (2005). Serial noninvasive photoacoustic imaging of neovascularization in tumor angiogenesis. Opt Express *13*, 89-95.
14. Zhang, Q., Iwakuma, N., Sharma, P., Moudgil, B.M., Wu, C., McNeill, J., Jiang, H., and Grobmyer, S.R. (2009). Gold nanoparticles as a contrast agent for in vivo tumor imaging with photoacoustic tomography. Nanotechnology *20*, 395102.
15. Jain, S., Hirst, D.G., and O'Sullivan, J.M. (2012). Gold nanoparticles as novel agents for cancer therapy. Br J Radiol *85*, 101-113.
16. Khlebtsov, N., and Dykman, L. (2011). Biodistribution and toxicity of engineered gold nanoparticles: a review of in vitro and in vivo studies. Chem Soc Rev *40*, 1647-1671.
17. Manohar, S., Ungureanu, C., and Van Leeuwen, T.G. (2011). Gold nanorods as molecular contrast agents in photoacoustic imaging: the promises and the caveats. Contrast Media Mol Imaging *6*, 389-400.
18. Luke, G.P., Myers, J.N., Emelianov, S.Y., and Sokolov, K.V. (2014). Sentinel lymph node biopsy revisited: ultrasound-guided photoacoustic detection of micrometastases using molecularly targeted plasmonic nanosensors. Cancer research *74*, 5397-5408.
19. Gobin, A.M., Lee, M.H., Halas, N.J., James, W.D., Drezek, R.A., and West, J.L. (2007). Near-infrared resonant nanoshells for combined optical imaging and photothermal cancer therapy. Nano letters *7*, 1929-1934.
20. Au, L., Zheng, D., Zhou, F., Li, Z.Y., Li, X., and Xia, Y. (2008). A quantitative study on the photothermal effect of immuno gold nanocages targeted to breast cancer cells. ACS nano *2*, 1645-1652.
21. Piao, J.G., Wang, L., Gao, F., You, Y.Z., Xiong, Y., and Yang, L. (2014). Erythrocyte membrane is an alternative coating to polyethylene glycol for prolonging the circulation lifetime of gold nanocages for photothermal therapy. ACS nano *8*, 10414-10425.
22. Weissleder, R., and Pittet, M.J. (2008). Imaging in the era of molecular oncology. Nature *452*, 580-589.
23. Jang, B., Park, J.Y., Tung, C.H., Kim, I.H., and Choi, Y. (2011). Gold nanorod-photosensitizer complex for near-infrared fluorescence imaging and photodynamic/photothermal therapy in vivo. ACS nano *5*, 1086-1094.
24. Liang, C., Diao, S., Wang, C., Gong, H., Liu, T., Hong, G., Shi, X., Dai, H., and Liu, Z. (2014). Tumor metastasis inhibition by imaging-guided photothermal therapy with single-walled carbon nanotubes. Advanced materials *26*, 5646-5652.
25. Xiao, Z., Ji, C., Shi, J., Pridgen, E.M., Frieder, J., Wu, J., and Farokhzad, O.C. (2012). DNA self-assembly of targeted near-infrared-responsive gold nanoparticles for cancer thermo-chemotherapy. Angewandte Chemie *51*, 11853-11857.
26. Ke, H., Yue, X., Wang, J., Xing, S., Zhang, Q., Dai, Z., Tian, J., Wang, S., and Jin, Y. (2014). Gold nanoshelled liquid perfluorocarbon nanocapsules for combined dual modal ultrasound/CT imaging and photothermal therapy of cancer. Small *10*, 1220-1227.

27. Shen, S., Kong, F., Guo, X., Wu, L., Shen, H., Xie, M., Wang, X., Jin, Y., and Ge, Y. (2013). CMCTS stabilized Fe3O4 particles with extremely low toxicity as highly efficient near-infrared photothermal agents for in vivo tumor ablation. Nanoscale *5*, 8056-8066.
28. Akhavan, O., and Ghaderi, E. (2013). Graphene nanomesh promises extremely efficient in vivo photothermal therapy. Small *9*, 3593-3601.
29. Antaris, A.L., Robinson, J.T., Yaghi, O.K., Hong, G., Diao, S., Luong, R., and Dai, H. (2013). Ultra-low doses of chirality sorted (6,5) carbon nanotubes for simultaneous tumor imaging and photothermal therapy. ACS nano *7*, 3644-3652.
30. Jensen, M.M., Jorgensen, J.T., Binderup, T., and Kjaer, A. (2008). Tumor volume in subcutaneous mouse xenografts measured by microCT is more accurate and reproducible than determined by 18F-FDG-microPET or external caliper. BMC medical imaging *8*, 16.
31. Zhang, M., Kim, H.S., Jin, T., Yi, A., and Moon, W.K. (2016). Ultrasound-guided photoacoustic imaging for the selective detection of EGFR-expressing breast cancer and lymph node metastases. Biomed Opt Express *7*, 1920-1931.
32. Cai, X., Li, W., Kim, C.H., Yuan, Y., Wang, L.V., and Xia, Y. (2011). In vivo quantitative evaluation of the transport kinetics of gold nanocages in a lymphatic system by noninvasive photoacoustic tomography. ACS nano *5*, 9658-9667.
33. Kobayashi, H., Kawamoto, S., Sakai, Y., Choyke, P.L., Star, R.A., Brechbiel, M.W., Sato, N., Tagaya, Y., Morris, J.C., and Waldmann, T.A. (2004). Lymphatic drainage imaging of breast cancer in mice by micro-magnetic resonance lymphangiography using a nano-size paramagnetic contrast agent. J Natl Cancer Inst *96*, 703-708.
34. Amersi, F., and Hansen, N.M. (2006). The benefits and limitations of sentinel lymph node biopsy. Curr Treat Options Oncol *7*, 141-151.
35. Bergkvist, L., Frisell, J., Swedish Breast Cancer, G., and Swedish Society of Breast, S. (2005). Multicentre validation study of sentinel node biopsy for staging in breast cancer. The British journal of surgery *92*, 1221-1224.
36. Ronka, R., Smitten, K., Sintonen, H., Kotomaki, T., Krogerus, L., Leppanen, E., and Leidenius, M. (2004). The impact of sentinel node biopsy and axillary staging strategy on hospital costs. Annals of oncology : official journal of the European Society for Medical Oncology / ESMO *15*, 88-94.
37. Chen, J., and Irudayaraj, J. (2009). Quantitative investigation of compartmentalized dynamics of ErbB2 targeting gold nanorods in live cells by single molecule spectroscopy. ACS nano *3*, 4071-4079.
38. Luke, G.P., and Emelianov, S.Y. (2015). Label-free Detection of Lymph Node Metastases with US-guided Functional Photoacoustic Imaging. Radiology *277*, 435-442.
39. Voduc, K.D., Cheang, M.C., Tyldesley, S., Gelmon, K., Nielsen, T.O., and Kennecke, H. (2010). Breast cancer subtypes and the risk of local and regional relapse. Journal of clinical oncology : official journal of the American Society of Clinical Oncology *28*, 1684-1691.
40. Sunada, H., Magun, B.E., Mendelsohn, J., and MacLeod, C.L. (1986). Monoclonal antibody against epidermal growth factor receptor is internalized without stimulating receptor phosphorylation. Proceedings of the National Academy of Sciences of the United States of America *83*, 3825-3829.
41. Al-Ejeh, F., Shi, W., Miranda, M., Simpson, P.T., Vargas, A.C., Song, S., Wiegmans, A.P., Swarbrick, A., Welm, A.L., Brown, M.P., et al. (2013).

Treatment of triple-negative breast cancer using anti-EGFR-directed radioimmunotherapy combined with radiosensitizing chemotherapy and PARP inhibitor. J Nucl Med *54*, 913-921.

42. Patra, C.R., Bhattacharya, R., Wang, E., Katarya, A., Lau, J.S., Dutta, S., Muders, M., Wang, S., Buhrow, S.A., Safgren, S.L., et al. (2008). Targeted delivery of gemcitabine to pancreatic adenocarcinoma using cetuximab as a targeting agent. Cancer research *68*, 1970-1978.
43. Overgaard, J. (1989). The current and potential role of hyperthermia in radiotherapy. International journal of radiation oncology, biology, physics *16*, 535-549.
44. Lepock, J.R. (2003). Cellular effects of hyperthermia: relevance to the minimum dose for thermal damage. International journal of hyperthermia : the official journal of European Society for Hyperthermic Oncology, North American Hyperthermia Group *19*, 252-266.
45. Wu, P., Gao, Y., Zhang, H., and Cai, C. (2012). Aptamer-guided silver-gold bimetallic nanostructures with highly active surface-enhanced Raman scattering for specific detection and near-infrared photothermal therapy of human breast cancer cells. Analytical chemistry *84*, 7692-7699.
46. Zou, L., Wang, H., He, B., Zeng, L., Tan, T., Cao, H., He, X., Zhang, Z., Guo, S., and Li, Y. (2016). Current Approaches of Photothermal Therapy in Treating Cancer Metastasis with Nanotherapeutics. Theranostics *6*, 762-772.

국문초록

서론: 에스트로겐 수용체(estrogen receptor: ER), 프로게스테론 수용체(progesterone receptor: PR) 발현 및 HER-2/neu 종양유전자 증폭이 없는 삼중음성 유방암은 유방암 아형 중 예후가 가장 나쁘다. 표피성장인자수용체(epidermal growth factor receptor, EGFR)는 70-80%의 삼중음성유방암에서 발현이 증가되어 있어 표적 진단과 치료를 위한 유전자로 제시되어 있다. 광음향영상은 다양한 생체내 또는 체외 광흡수 물질들을 감지하여 생체의 해부학적, 기능적, 대사적, 그리고 분자유전적인 특징을 영상으로 보여줌으로써, 비침습적 방법으로 고해상도 분자세포 영상 및 분광학 정보를 얻을 수 있으며 초음파와 결합이 용이하여 기초 연구뿐만 아니라 임상에서도 활용 가능한 영상기법이다. 본 연구에서는 EGFR항체접합 골드나노로드(anti-EGFR-GNs)와 광음향/초음파 일체형 영상기기를 사용하여 EGFR과발현한 유방암과 국소 림프절전이를 표적하여 진단하고, 근적외선을 병용하여 비침습적 열치료 효과를 실시간 모니터링하고 정량적으로 평가하였다.

실험방법: 사람유방암 세포주 (ER양성; MCF-7, HER2양성; BT-474, 삼중음성; Hs578T, HCC-38, HCC-1937, MDA-MB-468, MDA-MB-231)를 사용하였고 Western blot을 통해 각 세포에서의 EGFR 발현양을 확인하였다. MCF-7과 MDA-MB-231세포에 각각 GNs 와 anti-EGFR-GNs를 처리하여 EGFR표적지향성을 평가하였고 근적외선 열치료 병용 전후 세포 내 신호변화, 세포증식 및 세포자멸을 Western blot, MTT 및 유세포분석을 통하여 대조군과 비교 분석하였다. MCF-7과 MDA-MB-231세포를 면역결핍마우스 (BALB/c nude)의 피하에 이식하여 종양을 유발한 다음 0.5 pmol/g농도의 GNs와 anti-EGFR-GNs를 각각 마우스의

꼬리정맥으로 투여하여 광음향/초음파영상을 획득하고 광음향영상 신호강도를 분석하였다. 또한 MDA-MB-231 종양의 국소림프절전이 여부를 진단하기 위하여 MDA-MB-231 종양내에 anti-EGFR-GNs를 투여 후 림프절에서 광음향영상 신호 강도와 생체발광영상 신호 강도를 분석하였다. 마지막으로 삼중음성유방암 진단과 치료효과를 동시에 평가하기 위해서 anti-EGFR-GNs 와 근적외선 열치료를 단독 및 결합하여 체외와 체내에서 치료효과를 비교 분석하였다. 체내 모든 실험은 광음향 초음파 일체형 장비인 Vevo 2100 LAZR을 사용하였고 영상후처리 소프트웨어를 사용하여 통계분석 하였다. 영상 촬영이 끝난 후 조직을 적출하여 H&E염색, 은염색, 조직면역염색 및 TUNEL염색을 진행하였다.

결과: Western blot을 통해 삼중음성유방암세포(Hs578T, HCC-38, HCC-1937, MDA-MB-468 과 MDA-MB-231)가 다른 아형 유방암세포 (MCF-7, BT-474)에 비해 EGFR 발현양이 높은 것을 확인하였고 EGFR표적지향성을 평가한 결과 anti-EGFR-GNs가 GNs에 비해, MDA-MB-231에서 선택적으로 결합 되는 것을 광음향 영상, 전자현미경이미지 및 면역염색을 통하여 확인하였다. MDA-MB-231 종양과 MCF-7 종양에서 GNs와 anti-EGFR-GNs를 투여후 광음향신호를 분석한 결과 MDA-MB-231 종양에서는 GNs를 투여한 그룹에 비해 anti-EGFR-GNs을 투여한 종양에서 유의하게 EGFR표적 조영증강 효과를 관찰할 수 있었으나 MCF-7 종양에서는 두 그룹에서 유의한 차이가 없었다. 또한, MDA-MB-231 세포의 국소 림프절전이가 있는 마우스에서도 anti-EGFR-GNs 주사 24시간후, 전이림프절에서 현저한 조영증강 효과를 관찰할 수 있었다. anti-EGFR항체 단독 치료, anti-EGFR-GNs 단독 치료, anti-EGFR-GNs 와 근적외선 열치료를 병용하여 치료한 그룹을 체외와 생체내에서 치료효과를 분석한 결과, anti-EGFR-GNs 단독 치료한 그룹보다 열치료를 병용한 그룹에서 HSP70과 cleaved caspase-3를 더 많이 유도했고 Ki-67과 EGFR 를 더 많이 감소하였으며 EGFR관련 신호인 mTOR, AKT, ERK1/2,

FAK 인신화를 현저하게 차단하는 것을 확인하였다. 광음향/초음파와 생체발광 영상으로 실시간 모니터링한 결과 **anti-EGFR-GNs** 와 열치료를 병용한 그룹에서 종양성장이 억제되고 종양크기가 가장 많이 감소하여 성공적인 종양 치료효과를 확인하였다.

결론: 본 연구 결과를 통해 anti-EGFR-GNs와 광음향영상기법을 이용하여 삼중음성유방암을 선택적으로 표적 진단할 수 있었고 국소 림프절 전이여부도 확인 할 수 있었으며 또한 근적외선 열치료를 병용하여 치료효과도 모니터링 할 수 있었다. 본 연구에서 제시한 종양표적항체-나노로드 접합체를 사용한 광음향영상진단법과 근적외선 열치료의 병용치료법은 향후 삼중음성유방암의 표적 진단과 치료에 사용될 수 있을 것이다.

주요어: 광음향 영상, 골드나노로드, 표피성장인자, 초음파, 림프절전이, 삼중음성유방암, 근적외선, 열치료

학번: 2014-30871